Impact of genomic background and developmental state on signaling pathways and response to therapy in glioblastoma patient-derived cells

Artem Berezovsky[1,2¶], Oluwademilade Nuga[1,3¶], Indrani Datta[1], Kimberly Bergman[1], Thais Sabedot[1], Katherine Gurdziel[3,4], Susan Irtenkauf[1], Laura Hasselbach[1], Yuling Meng[1], Claudius Mueller[5], Emanuel F. Petricoin III[5], Stephen Brown[6], Neeraja Purandare[4], Sidhesh Aras[2,4], Tom Mikkelsen[7], Laila Poisson[8], Houtan Noushmehr[1], Douglas Ruden[4,9], Ana C. deCarvalho[1,2,3,10*]

[1]Department of Neurosurgery, Henry Ford Health, Detroit, Michigan, United States of America

[2]Department of Oncology, Wayne State University, Detroit, Michigan, United States of America

[3]Department of Pharmacology, Wayne State University, Detroit, Michigan, United States of America

[4]Institute of Environmental Health Sciences, Wayne State University, Detroit, Michigan, United States of America

[5]Center for Applied Proteomics and Molecular Medicine, George Mason University, Manassas, Virginia, United States of America

[6]Department of Radiation Oncology, Henry Ford Health, Detroit, Michigan, United States of America

[7]Precision Medicine Program, Henry Ford Health, Detroit, Michigan, United States of America

[8]Department of Public Health, Henry Ford Health, Detroit, Michigan, United States of America

[9]Department of Obstetrics and Gynecology, School of Medicine, Wayne State University, Detroit, Michigan, United States of America

[10]Department of Physiology, College of Human Medicine, Michigan State University, East Lansing, Michigan, United States of America

¶ These authors contributed equally to this work.

*Corresponding author; E-mail: decarva2@msu.edu (ACD)

Abstract

Glioblastoma (GBM) tumors represents diverse genomic epigenomic, and transcriptional landscapes, with significant intratumoral heterogeneity that challenges standard of care treatments involving radiation (RT) and the DNA-alkylating agent temozolomide (TMZ). In this study, we employed targeted proteomics to assess the response of a genomically-diverse panel of GBM patient-derived cancer stem cells (CSCs) to astrocytic differentiation, growth factor withdrawal and traditional high fetal bovine serum culture. Our findings revealed a complex crosstalk and co-activation of key oncogenic signaling in CSCs and diverse patterns of response to these external stimuli. Using RNA sequencing and DNA methylation, we observed common adaptations in response to astrocytic differentiation of CSCs across genomically distinct models, including BMP-Smad pathway activation, reduced cholesterol biosynthesis, and upregulation of extracellular matrix components. Notably, we observed that these differentiated CSC progenies retained a subset of stemness genes and the activation of cell survival pathways. We also examined the impact of differentiation state and genomic background on GBM cell sensitivity and transcriptional response to TMZ and RT. Differentiation of CSCs increased resistance to TMZ but not to RT. While transcriptional responses to these treatments were predominantly regulated by p53 in wild-type p53 GBM cells, its transcriptional activity was modulated by the differentiation status and treatment modality. Both mutant and wild-type p53 models exhibited significant activation of a DNA-damage associated interferon response in CSCs and differentiated cells, suggesting this pathway may play a wider role in GBM response to TMZ and RT. Our integrative analysis of the impact of GBM cell developmental states, in the context of genomic and molecular diversity of patient-derived models, provides valuable insights for pre-clinical studies aimed at optimizing treatment strategies.

Introduction

Glioblastoma (GBM), classified as World Health Organization (WHO) Grade 4 isocitrate dehydrogenase (IDH)-wildtype astrocytoma, remains the most aggressive and prevalent primary brain tumor in adults [1]. Since 2005, standard of care treatment of GBM includes maximal safe surgical resection [2], followed by ionizing radiation therapy (RT) and the brain-penetrant DNA-alkylating agent temozolomide (TMZ) [3]. Surgery alone is not curative [2] and TMZ provides a modest, significant increase in median overall survival in patients with newly diagnosed GBMs when combined with RT compared to RT alone [4]. TMZ sensitivity in newly diagnosed GBMs is modulated by the expression of DNA repair protein, O-6-methylguanine-DNA methyltransferase (MGMT). The silencing of MGMT through promoter hypermethylation is a predictive marker of TMZ sensitivity for newly diagnosed GBMs [5], while MGMT expression is also regulated by DNA methylation independent mechanisms [6, 7]. Most GBM patients have known actionable therapeutical targets [8], clinical trials for targeted therapies have not demonstrated sufficient efficacy in improving overall and progression-free survival [9].

Intra-tumoral heterogeneity (ITH) is a key factor contributing to GBM resistance to treatment and high recurrence rate. Genomically-defined subclonal populations presenting differential sensitivity to pharmacological agents can arise in post-treatment recurrent GBMs [10]. Another contributor to ITH is oncogene amplification in extrachromosomal DNA (ecDNA), as we previously reported cases of low frequency ecDNA in newly diagnosed GBM exhibiting a notable increase in prevalence at recurrence following treatment [11]. Non-genetic factors also contribute to ITH, such as the high degree of plasticity of GBM cells, reflected in the ability to transition into a continuum of cell states analogous to neural development, from neural stem/progenitor-like to differentiated astrocyte-like cells, as shown by bulk tumor RNA sequencing (seq) deconvolution and single cell RNAseq analyses [12]. ITH involves dynamic shifts in subclonal composition in response to treatment and to changes in the microenvironment in GBM [13, 14]. Thus, it is

88 important to consider ITH when designing preclinical studies to test optimization of treatment
89 efficacy for GBMs.

90 Tumor cell subpopulations exhibiting cancer stem cell-like (CSC) properties contribute to
91 another layer of ITH through developmental cell state plasticity [15]. Long-term self-renewal in
92 culture and the ability to differentiate and recapitulate the original tumor upon orthotopic
93 implantation in immunocompromised rodents are defining attributes of cancer stem cells (CSCs)
94 [16, 17]. These properties make CSCs invaluable for developing GBM patient-derived models for
95 pre-clinical studies. An established strategy to select for GBM CSC from surgical samples involves
96 culturing dissociated tumor cells in selective serum-free media, originally formulated for the
97 isolation of mouse neural progenitor cells, resulting in “neurosphere” cultures [18, 19]. In recent
98 years, GBM neurosphere cultures have been extensively validated as a renewable source of
99 patient-derived neoplastic cells retaining remarkable genomic fidelity to the original tumor [11, 20,
100 21]. These neurosphere/CSC cultures are amenable to in vitro biological and experimental
101 therapeutics studies [22] and are suitable for validation in xenografts. To enhance the translational
102 applicability of in vitro investigations aimed at optimizing treatment efficacy in GBMs, it is
103 imperative to consider the influence of patient genomic diversity and intra-tumoral phenotypic
104 variability. Ultimately, the diversity in genomic and epigenomic drivers among GBM patients, along
105 with the additional variability associated with dynamic ITH, converge on the deregulation of key
106 oncogenic signaling involving receptor tyrosine kinases (RTK), phosphoinositide 3-kinases
107 (PI3K)- protein kinase B (AKT)- mammalian target of rapamycin (mTOR) and mitogen-activated
108 protein kinase (MAPK) pathways. These pathways are deregulated in 90% of GBM patients [23],
109 and cross activation of PI3K and MAPK contribute to several aspects of GBM malignancy [24].

110 The objective of this study is to investigate the contributions of somatic genomic alterations
111 in conjunction with GBM cellular developmental states to the modulation of key signaling
112 pathways and response to TMZ and RT. Employing targeted proteomics, we assessed changes
113 in the steady-state levels of key oncogenic signaling components, following a 2-week exposure

114 of CSCs to astrocytic differentiation (SDCs), growth factor withdrawal, or traditional culture media
115 supplemented with 10% FBS. in a genomically-diverse panel of CSCs derived from newly
116 diagnosed GBM patients [11, 25, 26]. The representation of various genomic backgrounds and
117 external stimuli in the targeted proteomics dataset provided insights into the complex signaling
118 networks co-activated in GBMs, while uncovering a strong positive correlation between NF-kB
119 activation and MGMT protein expression, regardless of MGMT promoter methylation status.
120 Some of the signaling and transcriptional program adaptations in response to astrocytic
121 differentiation of CSCs were shared among the genomically distinct models, including BMP-Smad
122 pathway activation, decrease in cholesterol biosynthesis, increase in extracellular matrix (ECM)
123 production, and retention of the expression of a subset of stemness genes. Other CSC
124 differentiation mediated alterations were tumor specific, such as activation of the interferon (IFN)
125 response. Here, we show that differentiation of CSCs increases resistance to TMZ but not to RT,
126 and that transcriptional responses to these treatments are largely regulated by p53 in wildtype
127 (wt) p53 GBM cells and modulated by cell differentiation state. In both mutant and wt p53 models,
128 we observed prominent activation of DNA-damage associated IFN response. We show that
129 modeling the differentiation of GBM CSCs in vitro provides a powerful platform to uncover the
130 interaction of genomic landscape and cell state on signaling pathways and response to treatment.
131

132 # Results

133 ## Alterations in key cell signaling pathways in glioblastoma
134 ## cancer stem cells in response to astrocytic differentiation,
135 ## growth factor withdrawal and traditional 10% FBS media.

136 CSCs derived from 8 newly diagnosed GBM patients, representing the main genomic
137 drivers were selected for this study (Fig 1A). These CSC lines meet the requirement of the two
138 defining stemness criteria: long term self-renewal and orthotopic tumor formation in

139 immunocompromised mice [11, 25, 26]. FBS, a supplement supporting the culture of a variety of
140 mammalian cells, contains hormones, growth factors, cell attachment factors and other nutrients
141 [27]. Media supplemented with 10% FBS had been widely employed to propagate glioma cells in
142 culture, prior to seminal data demonstrating genetic drift occurring from serial passaging under
143 these conditions [28]. In contrast, 1-2% FBS added to defined media has been successfully used
144 to differentiate human-induced pluripotent stem cells (hiPSC)-derived neural stem cells into
145 astrocytic lineage [29, 30]. Using this paradigm to model a differentiated phenotype in culture,
146 CSCs growing in 3D cultures in defined neurosphere media, supplemented with, 20 ng/ml each
147 epidermal (EGF) and basic fibroblast (bFGF) growth factors (NMGF), were differentiated into an
148 astrocytic phenotype in NMGF supplemented with 2% FBS for 14 days. This differentiated CSC
149 progeny is referred to here as “serum differentiated cells” (SDC). For comparison, we tested two
150 additional growth conditions: growth factor-depleted neurosphere media (NM), or media
151 supplemented with 10% FBS (10% FBS) (Fig 1B). After 2 weeks in culture, cell lysates were
152 obtained and analyzed by Reverse Phase Protein Arrays (RPPA) in triplicates, as described [31,
153 32]. The levels of 66 proteins or post-translational modifications (PTM) in the cell lysates were
154 quantified (S1 Table). Pairwise comparisons between NMGF (CSC) culture and either NM or 2%
155 FBS (SDC) for the 8 cell lines did not show a global shift in the levels of protein/PTMs levels
156 (S1_Fig), but important patterns of alteration in specific signaling were observed. Phosphorylation
157 (phospho) levels of serine (Ser)-residues in receptor-dependent r-Smad1/5/8, which are primarily
158 activated by BMP ligand signaling, were notably upregulated in SDCs in relation to CSCs in all 8
159 GBM models (Fig 2A). Consistent with bone morphogenetic protein (BMP) ligands being present
160 in FBS [33], increased levels of p-Smad1/5/8 were also observed in 10% FBS cultures for all
161 models (S1 Table). The tumor suppressor phosphatase and tensin homolog (PTEN) function is
162 frequently lost in GBMs through gene deletion and mutations, as seen in 7/8 GBM tumors
163 represented in this study (Fig 1A), leading to activation of AKT[34]. AKT phosphorylation at both
164 Y308 (by pyruvate dehydrogenase kinase 1 (PDK1)) and S473 (by mammalian target of

165 rapamycin complex 2 (mTORC2)) was suppressed in the absence of growth factors (NM) for all
166 lines, except for HF2927, which carries ligand independent epidermal growth factor receptor
167 (EGFR) variant III (viii) amplification. In 2% FBS (SDCs), AKT phosphorylation was suppressed
168 for HF2587, HF3035 and HF3077, and upregulated or unchanged in the remaining models (Fig
169 2A). In response to growth factor withdrawal, phosphorylation levels of S6 ribosomal proteins
170 (RBS6), downstream of mTORC1, were decreased while phospho- extracellular signal-regulated
171 kinases **(**ERK) increased for most CSC lines (Fig 2A). Phospho-EGFR (Y1173 and Y1068) levels
172 were increased in response to growth factor withdrawal exclusively in the EGFRvIII line HF2927
173 (Fig 2A). Expression of MET proto-oncogene, receptor tyrosine kinase (cMET) was observed for
174 all CSCs (S1 Table), but in the absence of MET ligand (hepatocyte growth factor) in the media,
175 only HF2927 and HF3016 presented modest levels of MET activation, which was suppressed in
176 2% FBS (Fig 2A).

177 We used this unique targeted proteomics dataset, integrating various genomic
178 backgrounds and culture conditions, to further investigate the signaling networks in glioblastoma.
179 The Spearman correlation of key proteins and post-translational modifications levels in all 96
180 samples (8 GBM lines in 4 media conditions in triplicate) was calculated and displayed in the
181 heatmap (Fig 2B). Glycogen synthase kinase-3 (GSK3)α/β is a multifunctional kinase frequently
182 inhibited by phosphorylation downstream of PI3K/AKT, mTORC1 or MAPK signaling. Here, we
183 observed that phosphorylation of GSK3α/β at S21/S9 was strongly correlated with AKT activation
184 (Fig 2B). While mTORC1 is activated by AKT [35], in this dataset AKT activation did not correlate
185 with markers of mTORC1 signaling, such as mTOR phosphorylation at the C-terminus S2448
186 residue [36], p70 ribosomal protein S6 kinase 1 (S6K) phosphorylation at T412, or
187 phosphorylation of RBS6 [37] (Fig 2B). On the other hand, phosphorylation of AMP-activated
188 protein kinase (AMPK) subunit β1 at S108 was highly correlated with mTORC1 activation (Fig
189 2B). AMPK αβɣ heterotrimeric complex is activated in response to low oxygen, low nutrients, and
190 DNA damage, playing important roles in cancer [37] . AMPK is inactivated by AKT phosphorylation

191 of AMPKα1 at S485 residue, while phosphorylation at AMPKβ1 S108 sensitizes AMPK to agonists
192 [38], having a function in pro-survival pathways [39]. SRC proto-oncogene, non-receptor tyrosine
193 kinase (Src) is a node of convergence for receptor mediated signaling pathways, activating
194 substrates in the MAPK, JAK/Stat3, and PI3K/AKT pathways to promote tumor cell survival,
195 proliferation and invasion in various cancers, including GBMs [40]. Src activity is inhibited by
196 phosphorylation of Y527 by C-terminal Src kinase (CSK) and regulated by dephosphorylation by
197 protein tyrosine phosphatases (PTPs), leading to conformational change and
198 autophosphorylation of Y416 [41]. Levels of inhibitory Src phospho-Y527 were elevated in
199 HF2354, HF2587, HF3016 and HF3077 relative to other CSC lines while the levels of Src
200 phospho-Y416 were less variable among CSC lines and media conditions (S1 Table) and
201 positively correlated with Src phospho-Y527 (r=0.705, CI: 0.584 to 0.796) but not with phospho-
202 signal transducer and activator of transcription 3 (Stat3 S727), a canonical downstream signal
203 transducer (Spearman correlation, r=0.302, CI: 0.1026 to 0.4788) (Fig 2B). This bi-
204 phosphorylation of Src has been previously reported to reflect an intermediate state between open
205 and closed kinase conformations with blockage of the SH3 domain leading to limited Stat3
206 phosphorylation activity, suggesting that additional stimulatory factors are required for
207 downstream signaling [42]. Phospho-Stat3 was positively correlated with mTORK1 (phospho-
208 mTOR, phospho-SK6) and MAPK (phospho-RSK) signaling (Fig 2B). Signaling through insulin
209 like growth factor 1 receptor (IGF1R) and insulin receptor (IR) promotes cancer cell proliferation,
210 survival, and treatment resistance in diverse malignancies. Upon ligand binding, IGF1R
211 homodimer or IGF1R/IR heterodimer receptors recruit insulin receptor substrate (IRS) adaptor
212 protein to transduce downstream signaling through binding of src-homology-2 (SH2) proteins,
213 such as p85 to activate PI3K and growth factor receptor bound protein 2 (GRB2) to activate ERK
214 [43]. All four media conditions tested here contain insulin at a final concentration of 50 μg/ml (N2
215 supplement), which has been shown to activate IGF1R, although at a lower rate than the
216 canonical ligand IGF2 [44], while the FBS supplemented media contains additional insulin and

217 IGF1/2 ligands [27]. Consistently, activation of IGF1R (phospho-Y1135/Y1136) /IR (phospho-
218 Y1150/Y1151) presented little variation among GBM lines and culture conditions (S1 Table).
219 mTORC1 phosphorylates IRS1 at S616 residue leading to the adaptor turnover [45], but p-IRS1
220 did not correlate with mTORC1 activation. Instead, a strong correlation of p-IRS1 with inactivating
221 phosphorylation of forkhead box protein O1 (FOXO1/FKHR) on S256, which is attributed to AKT
222 [46], was observed (Fig 2B). This targeted proteomics analysis using genomically diverse patient
223 samples in different culture conditions reveled a complex pattern in the integration of signaling
224 cascade nodes, likely reflecting deregulation of multiple oncogenic pathways observed in GBMs.
225 Z-scores were calculated for each protein/PTM based on its distribution across all 8
226 models and 4 media conditions, and cumulative z-scores were determined for key signaling
227 pathways and cellular functions (S1 Table). Interestingly, we observed a remarkable pattern of
228 inhibition for key signaling pathway and functions in 10% FBS, in contrast with 2% FBS (SDC)
229 cultures (Fig 3A), further corroborating the inadequacy of culturing GBM cells in 10% FBS [28,
230 47]. Receptor tyrosine kinase activation ("RTK") index, based on the levels of Tyr phosphorylation
231 corresponding to activation of 11 RTKs (S1 Table), decreased in 2% FBS (SDCs) relative to CSCs
232 in HF2927 and HF3016, the only 2 models harboring EGFR amplification on extrachromosomal
233 DNA (ecDNA) [11], and increased in the remaining 6 GBM models (Fig 3A). The levels of EGFR
234 were 10-fold higher for HF2927 CSCs, which also carries the EGFRvIII variant (Fig 1A), relative
235 to HF3016, while the levels of phospho-EGFR at carboxy-terminal Y1068 and Y1173 residues
236 were comparable for these 2 CSC lines (Fig 3A). Interestingly, EGF withdrawal for 2 weeks (NM)
237 led to a 4-fold increase in the levels of EGFR activation in HF2927 (S1 Table, Fig 2A), suggesting
238 an inhibitory effect of long-term exposure to EGF ligand on EGFRvIII. RTK activation correlated
239 with downstream RTK signaling pathway ("TK_Signaling"), which includes both MAPK and
240 PI3K/Akt/mTOR ("PI3K") pathways (Fig 3A). As part of RTK signaling convergence, SHC Adaptor
241 Protein 1 (SHC1) binds to phosphorylated EGFR Y1173, which is further phosphorylated on Y239
242 and Y317 resulting in recruitment of Grb2 and downstream activation of MAPK and PI3K/AKT

243 pathways [46]. Phospho-Shc1 (Y317) was only observed for HF2927 and HF3016 CSCs, and in
244 both cases upregulated upon growth factor withdrawal (NM) and downregulated in the presence
245 of FBS, following the pattern of EGFR activation (S1 Table, Fig 2A). MAPK signaling activation
246 and cytoskeletal function, consisting of regulation of actin and microtube dynamics (S1 Table),
247 were maintained or increased in SDCs for all models except HF2927 and HF3016 (Fig 3A),
248 analogous to what we observed for the RTK index. The PI3K/AKT/mTOR pathway activation
249 score was low for HF2927 CSCs, relative to the other CSC lines, and remained low in NM and
250 2% FBS, despite genomic loss of PTEN, EGFRvIII amplification, and high level of EGFR
251 activation (Fig. 3A). PI3K/AKT/mTOR activation index was higher for the other 7 CSCs,
252 maintained in SDCs, and decreased in the absence of growth factors (Fig. 3A).

253 Since several of these signaling pathways are involved in cell survival and proliferation,
254 we established a cell "viability index" measuring the net result from the sum of the level of
255 protein/PTM associated with cell survival and proliferation minus the level of markers associated
256 with programed cell death (S1 Table). We observed that the viability index varied among CSC
257 lines and was not impacted by culture conditions in the same pattern, decreasing in SDC in half
258 of the models and increasing in the other half. (Fig 3A). Three models, HF2303, HF2927 and
259 HF3016, representing each of the 3 transcriptional subclasses, diverse genomic features (Fig
260 1A), and a range of viability index values, were selected for further characterization. Levels of
261 individual protein/PTM associated with cell death and survival are shown (Fig 3B). High PTEN
262 expression was observed in HF2303, harboring pathogenic p.D92E mutation in the WPD loop
263 [48], corresponding to a high level of phosphorylation at S380 in the carboxy terminal tail, a crucial
264 post-translational modification for blocking proteasomal degradation [49]. High levels of AKT
265 activation observed for HF2303 CSCs were further increased in SDCs, indicating that the p.D92E
266 mutation impairs PTEN ability to inhibit AKT. Conversely, PTEN levels were very low in HF3016,
267 which carries a pathogenic mutation in the P-loop, p.I122S [48], comparable to PTEN-null HF2927
268 (Fig 3B). Increased levels of phospho-ERK and phospho- c-Jun N-terminal kinase (JNK) were

269 observed for HF2303 and HF2927 in response to growth factor withdrawal (NM), and in HF2303,
270 the increase was also observed in SDCs, relative to CSCs. The levels of p53 protein were
271 consistent with the mutation status for these lines (Fig 3B). Thus, our comparative analysis
272 confirms that at the individual protein/PTM levels, differences in pathways regulating cell survival
273 and death in untreated GBM cells are largely determined by the genomic landscape, with cell
274 state playing a lesser role.

275 CSC presents increased sensitivity to temozolomide but not 276 to radiation compared to their SDC progeny.

277 MGMT epigenetic silencing is a clinically used biomarker to predict response to TMZ
278 treatment. HF3016 and HF2303 CSCs were derived from tumors with unmethylated and HF2927
279 CSC from a tumor with methylated MGMT promoter (Fig. 1A). Accordingly, HF2927 cells
280 presented the lowest level of MGMT protein. Despite both having unmethylated promoter status,
281 MGMT levels were 2.5-fold higher for HF3016 relative to HF2303 (Fig. 4A, S1 Table). MGMT
282 protein level in HF2303 was unchanged among all three culture conditions, while MGMT was
283 significantly downregulated in SDCs relative to CSCs for HF2927 and HF3016 (Fig 4A). We
284 confirmed that MGMT promoter was unmethylated for HF2303 and methylated for HF2927 cells
285 and did not observe changes in methylation between CSC and SDCs for either of these models
286 (S2 Fig). DNA methylation data is unavailable for HF3016 SDCs, preventing us from entirely ruling
287 out differentiation-mediated alterations in MGMT promoter methylation in this model. We
288 observed that MGMT protein expression pattern in the two models with unmethylated promoter,
289 HF3016 and HF2303 (Fig 4A), was highly correlated (Spearman r =0.823; 95% CI: 0.6213 to
290 0.9228) with the levels of activated nuclear factor-kappa B (NF-kB) p65 (phospho-S536) (Fig 3B,
291 S1 Table). Remarkably, the correlation between activated NF-kB and MGMT levels was
292 significant for all models, regardless of promoter methylation status, but stronger for those
293 presenting unmethylated MGMT (Fig 4B). To investigate to what extent the developmental state
294 affected the sensitivity of GBM cells to genotoxic treatments, HF2303, HF2927 and HF3016

295 CSCs, along with their SDC progenies, were treated with TMZ and RT (Fig 1C). These models
296 represent diverse molecular characteristics known to modulate response to DNA-damaging
297 agents, such as TP53 status and MGMT promoter methylation. First, we compared cell
298 proliferation rates between 3D CSC and 2D SDC cultures. SDCs proliferated at a higher rate than
299 CSCs for HF3016 only, while no significant difference was observed for the other two lines (Fig
300 5A). Cells were then treated for 4 days with doses ranging from 0 (DMSO) to 400 mM TMZ, in
301 quintuplicates. To compensate for possible binding of TMZ by proteins in FBS, even at the low
302 concentration used, the serum-free neurosphere media was supplemented with bovine serum
303 albumin (1%) [50]. Half maximal inhibitory concentration (IC50) and area above the curve (AAC)
304 were calculated from dose-response curves generated by non-linear fitting. HF2927 cells were
305 more sensitive to TMZ in comparison with the other two cell lines (Fig 5B), as expected based on
306 MGMT promoter methylation and expression (Fig 4A). Differentiation of CSCs into SDCs
307 significantly increased resistance to TMZ for all three lines (Fig 5B), despite downregulation of
308 MGMT protein observed for HF2927 and HF3016 SDCs (Fig 4A).

309 We then compared the sensitivity of CSCs and SDCs to clinically relevant RT doses.
310 Isogenic populations of CSCs and their SDC progenies were exposed to 2 gray (Gy) and 4 Gy
311 RT doses and cultured for 5 days, surviving fractions (SF2 and SF4) relative to control treatment
312 were determined (Fig 6A) as previously described [51]. Sensitivity to RT was variable among
313 these models, as a high degree of resistance was observed for HF2303 cells relative to both
314 HF3016 and HF2927; HF2927 was the most sensitive (Fig 6A). On the other hand, no significant
315 difference in sensitivity to RT between CSCs and SDCs were observed for these three models
316 (Fig 6A). To evaluate the long-term effect of radiation, we compared the tumorigenic potential of
317 control and RT treated CSCs. Cells expressing firefly luciferase (fLuc) were implanted
318 intracranially in nude mice immediately after radiation (4 Gy), or mock radiation (control). Tumor
319 growth was monitored by weekly bioluminescence imaging and by daily monitoring of symptoms
320 associated with tumor burden. The three irradiated CSC lines exhibited a delay in tumor growth

321 relative to controls, assessed by symptom-free survival, with all mice eventually developing
322 tumors, demonstrating that cells surviving 4 Gy RT dose were tumorigenic. HF2303 displayed the
323 highest resistance to RT in vitro and exhibited the least significant difference in the survival curves.
324 On the other hand, the HF2927 cells, which were the most sensitive to RT in vitro, displayed the
325 lowest p-value in the curve comparison (Fig 6B,C). The degree of difference in survival curves
326 (Log-rank p-values) ranked according to the in vitro sensitivity of each cell line to RT.

327 Transcriptional reprogramming in response to CSC 328 differentiation

329 To determine how differentiation state impacts transcriptional reprogramming in response
330 to TMZ and RT, we selected the most resistant (HF2303) and the most sensitive (HF2927)
331 models. We first determined the pattern of global transcriptome changes after differentiation of
332 CSCs into SDCs from bulk RNAseq data. To identify differentially expressed genes between the
333 two differentiation states, we employed the non-parametric NOISeq R package, and subsequently
334 performed pathway enrichment analysis, as detailed in the Materials and Methods section.
335 Numerous signaling pathways and cellular processes enriched in CSCs were cell line specific. It
336 has been proposed that CSCs, from GBMs and other cancers, tend to rely more on oxidative
337 phosphorylation (OXPHOS) than the more differentiated cancer cells [52]. Here, we observed that
338 OXPHOS gene expression signature was enriched in HF2303 CSCs but not HF2927 CSCs (Fig
339 7A). Interestingly, reserve respiratory capacity was higher in untreated HF2303 relative to HF2927
340 cells, and higher in SDC compared to CSCs (S3 Fig). Replication-dependent histones were highly
341 enriched in HF2303 CSCs, in the absence of enrichment in cell proliferation markers (Fig 7A, S2
342 Table), as previously observed for embryonic and induced pluripotent stem cells [53]. Several
343 nuclear pseudogenes with sequence similarity to mitochondrially encoded 16S rRNA (e.g.
344 *MTRNR2L1, MTRNR2L3*), enriched in HF2303 CSCs (A in S2 Table) are predicted to encode
345 humanin-like peptides and to be involved in negative regulation of the execution phase of
346 apoptosis [54] (Fig 7A). IL2-STAT5 signaling was specifically upregulated in HF2927 CSC in

347 relation to SDC (Fig 7A), in agreement with levels of pSTAT5_Y694 being elevated in HF2927
348 CSC (4.697 ± 0.98), while undetectable in HF2927 SDCs and HF2303 cells (B in S1 Table).
349 Patterns of transcriptome reprogramming in response to differentiation that were common to both
350 HF2927 and HF2303 models included downregulation of genes involved in cholesterol
351 biosynthesis and upregulation of genes associated with ECM components and organization,
352 including collagen type IV alpha 6 chain (*COL4A6*), a target of SRY-box transcription factor 2
353 (*SOX2*) transcriptional regulation [55] (Fig 7B). The expression of several transcription factors
354 associated with stemness and pluripotency, such as *SOX2,* spalt like transcription factor 2
355 (*SALL2*) and POU class 5 homeobox 1 (*POU5F1* (Oct3/4)), was not altered upon differentiation
356 of HF2303 and HF2927 CSCs into SDCs (A,B in S2 Table).On the other hand, other neural
357 progenitor and stemness markers expressed in CSCs were down regulated upon differentiation:
358 oligodendrocyte transcription factor 1 (*OLIG1*) in both lines; delta like canonical Notch ligand 3
359 (*DLL3*), integrin subunit alpha 6 (I*TGA6*), ETS variant transcription factor 4 (*ETV4*) in HF2927;
360 fatty acid binding protein 7 (*FABP7*), oligodendrocyte transcription factor 2 (*OLIG2*) and ELOVL
361 fatty acid elongase 2 (*ELOVL2*) [56] in HF2303 (Fig 7A, B).

362 IFN and interleukins signaling were specifically upregulated in HF2303 SDCs (Fig 7C).
363 Indeed 29 genes associated with IFN response pathways were upregulated in HF2303 SDCs
364 (Table 1), including members of the 49-gene interferon-related DNA damage resistance signature
365 (IRDS) [57]. Differentiation of CSCs into SDCs resulted in enrichment of the epithelial
366 mesenchymal transition (EMT) signature for HF2303 but not for HF2927 (Fig 7C), consistent with
367 the transcriptional subclasses affiliation, mesenchymal for HF2303 and classical for HF2927 (Fig
368 1A). In agreement with our observation that receptor dependent SMAD1/3/8 are activated in GBM
369 SDCs (Fig. 2A), inhibitor of DNA binding 1 (*ID1*), *ID2* and *ID3*, BMP/retinoic acid inducible neural
370 specific 1 (*BRINP1*), downstream of BMP signaling, were upregulated in HF2927 SDCs (Fig 7C).
371 Several components of the TGFb superfamily signaling were upregulated in HF2303 SDCs,
372 including transforming growth factor beta receptor 2 (*TGFBR2*), *BMP1*, latent transforming growth

373 factor beta binding protein 1 (*LTBP1*), *LTBP3*, *SMAD3*, *SMAD9* (Fig 7C,D; S2 Table). On the
374 other hand, endogenous *BMP4* mRNA was downregulated and BMP antagonists DAN family BMP
375 antagonist (*NBL1*) and BMP and activin membrane bound inhibitor (*BAMBI*) were upregulated in
376 HF2303 SDCs, suggesting a possible negative feedback loop, specific for this model. BAALC
377 binder of MAP3K1 and KLF4 (*BAALC)*, a regulator of developing neuroectoderm tissues
378 overexpressed in acute leukemia and GBM [58], and a target of SOX2 in differentiated GBM cells
379 [26], was upregulated in HF2303 SDCs (Fig 7C). Toll like receptor 4 (*TLR4*), which is expressed
380 in both immune and neoplastic cells, was also upregulated in HF2303 SDCs (Fig 7C), in
381 agreement with previous studies [59]. *HIF1A, an* IFN responsive gene (Table 1), along with
382 downstream hypoxia markers were uniquely upregulated in HF2927 SDCs, under normal oxygen
383 levels (Fig 7C)`. The 24 genes commonly upregulated in SDCs for both lines were enriched in
384 ECM components (Fig 7D). Small nucleolar RNAs were also upregulated upon differentiation of
385 both HF2303 and HF2927 (Fig 7D; S2 Table), including SNORD116 cluster, shown to have non-
386 canonical functions in the differentiation, survival, and proliferation of neuronal cells [60].

387 **Table 1. Differentially expressed genes associated with IFN response and signatures.**

Gene Symbol	DEG in response to 2% FBS differentiation		DEG in response to TMZ		DEG in response to RT		IFN response
	Upregulated	Downregulated	Upregulated	Downregulated	Upregulated	Downregulated	
ACSL5	-	-	HF2927 SDC	-	-	-	a
ODF3B	-	-	HF2927 SDC	-	-	-	a
NEAT1	-	-	HF2927 SDC	-	-	-	d
SECTM1	-	-	HF2927 SDC	-	-	-	c
OASL	-	-	HF2927 SDC; HF2927 CSC	-	-	-	a, b, c, d
CDKN1A	HF2303	-	HF2927 SDC; HF2927 CSC	-	-	-	c
RSAD2	-	-	HF2927 SDC; HF2303 SDC	-	-	-	a, b, c
CMPK2	-	-	HF2927 CSC	-	-	-	a, b, c
CXCL10	-	-	HF2927 CSC	-	-	-	a, b, c, d
EPSTI1	-	-	HF2927 CSC	-	-	-	a, b, c
DHX58	-	-	HF2927 CSC	-	-	-	a, b, c

MX2	-	-	HF2927 CSC	-	-	-	a, c, d
ISG15	HF2303	-	HF2927 CSC	-	-	-	a, b, c, d
TRIM22	-	-	HF2927 SDC; HF2927 CSC	-	HF2927 CSC	-	a
MX1	HF2303	-	HF2927 CSC; HF2303 CSC; HF2303 SDC	-	HF2927 CSC	-	a, b, c, d, e
IFI6	HF2303	-	HF2927 CSC	-	HF2927 CSC	-	a, d
OAS2	-	-	-	-	HF2927 CSC	-	a, c
HERC6	-	-	-	-	HF2927 CSC	-	a, b, c, d
IFI44L	-	-	-	-	HF2927 CSC	-	a, b, c, d
HLA-E	HF2303	-	-	-	HF2927 CSC	-	a
OAS1	-	-	HF2303 SDC	-	-	-	a, b, d, e
OAS3	-	-	HF2303 SDC	-	-	-	a, c, d
SAMD9L	-	-	HF2303 SDC	-	-	-	a, b, c
GIMAP2	-	-	-	HF2927 SDC	-	-	a
TNFAIP3	-	-	-	HF2927 SDC	-	-	c
THBS1	-	HF2927	-	HF2927 SDC	-	-	d
TNFAIP6	-	HF2927	-	HF2927 SDC	-	-	c
HLA-B	HF2303	-	-	-	-	HF2303 CSC	a, c, d
IGF2	-	-	-	-	-	HF2303 CSC	d
MTHFD2	-	HF2303	-	-	-	-	c
IFIT3	HF2303	-	-	-	-	-	a, b, c, d, e
BST2	HF2303	-	-	-	-	-	a, b, c, d
IFI44	HF2303	-	-	-	-	-	a, b, c, d, e
RIGI	HF2303	-	-	-	-	-	a, c
IRF9	HF2303	-	-	-	-	-	a, b, c
IFIT2	HF2303	-	-	-	-	-	a, b, c
IFITM1	HF2303	-	-	-	-	-	a. b. d
PLSCR1	HF2303	-	-	-	-	-	a, b, c, d
PLAAT4	HF2303	-	-	-	-	-	a
HLA-C	HF2303	-	-	-	-	-	a, b
LGALS3BP	HF2303	-	-	-	-	-	a, b, c, d
CA2	HF2303	-	-	-	-	-	d
ARL4A	HF2303	-	-	-	-	-	c
BTG1	HF2303	-	-	-	-	-	c
C1R	HF2303	-	-	-	-	-	c
CCL2	HF2303	-	-	-	-	-	c

FGL2	HF2303	-	-	-	-	-	c
ICAM1	HF2303	-	-	-	-	-	c
MVP	HF2303	-	-	-	-	-	c
NAMPT	HF2303	-	-	-	-	-	c
PELI1	HF2303	-	-	-	-	-	c
UPP1	HF2303	-	-	-	-	-	c
MT2A	HF2303	HF2927	-	-	-	-	c
HIF1A	HF2927	-	-	-	-	-	c

(a) S3_Table TCGA IFN response correlation group; (b) M5911 Hallmark IFN alpha response https://www.gsea-msigdb.org/; (c) M5913 Hallmark IFN gamma response https://www.gsea-msigdb.org/; (d) IRDS ref. [57]; (e) IFN/STAT1 survival proneural ref. [63]

Transcriptional response to sublethal treatment with temozolomide and radiation is determined by genomics and differentiation state.

To compare the transcriptional response to temozolomide treatment at distinct differentiation states, GBM cells were treated in triplicate with the respective TMZ IC40 concentrations, calculated from dose-response curves in Fig 5B: 58 mM (HF2303 CSC), 25 mM (HF2927 CSC), 134 mM (HF2303 SDC), 70 mM (HF2927 SDC), or equivalent DMSO control for 4 days. Cells were then harvested and total RNA isolated and sequenced. Differentially expressed genes between treated and control samples for each model and culture type were determined as described for Fig. 7 (C and D in S2 Table). Transcriptional response to 4-day TMZ treatment was largely regulated by wt p53 activation in HF2927 cells (Fig. 8A). We observed that 18 out of the 36 genes commonly upregulated in HF2927 CSCs and SDCs in response to TMZ treatment (Table 2) are direct transcriptional targets of p53 [55]. However, the differentiation state of HF2927 cells also influenced p53 transcriptional specificity, as 23 and 26 p53 target genes were significantly upregulated in response to TMZ exclusively in CSCs or SDCs, respectively (Table 2). In contrast, interleukin-27 (IL-27) mediated signaling pathway was enriched in HF2303 SDC in response to TMZ (Fig 8A), based on the upregulation of Myxovirus resistance dynamin like GTPase 1 (*MX1*), 2' 5' oligoadenylate synthetase 1 (*OAS1*) and *OAS2*, all of which are members of the IRDS [57],

407 providing further evidence for the proposed cooperation between IL-27 and IFN signaling in
408 response to DNA damage [61]. To identify other components of IFN signaling in GBMs, we
409 identified 100 genes whose expression presented the highest correlation to *OAS1* (Spearman's r
410 > 0.55; q value < 5.0E-12) in The Cancer Genome Atlas (TCGA) GBM data set (CBIOPortal [62],
411 accessed on 01/19/24). 62% of these genes are members of the hallmark IFN alpha or gamma
412 response pathways, 24% are members of the IRDS [57], and this gene list also includes the
413 IFN/STAT1 prognostic signature proposed for GBM proneural subtype [63] (S3 Table). We
414 observed activation of IFN response in TMZ-treated HF2927 CSCs and SDCs, and in HF2303
415 SDCs (Fig 8A, Table 1). TMZ treatment induced expression of ECM components, and several
416 neural developmental growth and survival factors, including brain derived neurotrophic factor
417 (*BDNF*) and glial cell derived neurotrophic factor (*GDNF*), in HF2927 CSCs and SDCs (Fig 8A).
418 Expression of other genes associated with neural development were down regulated in TMZ
419 treated HF2927: platelet derived growth factor receptor alpha (*PDGFRA*), *OLIG2*, and prominin 1
420 (*PROM1*) in SDCs; neuropilin 1 (*NRP1*), GLI family zinc finger 1 (*GLI1*), and Kruppel like factor 9
421 (*KLF9*) in CSCs (Fig 8A). *CDKN1A* (p21), the main effector of p53-mediated downregulation of
422 cell cycle genes, leading to cell cycle arrest, was upregulated in response to TMZ in both HF2927
423 CSCs and SDCs (Fig 8A,D). The more pronounced downregulation of cell cycle genes in HF2927
424 SDCs relative to CSCs (Fig 8A) is consistent with corresponding upregulation of Lin-37 DREAM
425 MuvB core complex component (*LIN37*)in SDC but not in CSC (Fig 8A), as LIN37 is required for
426 transcriptional repression by the DREAM complex, downstream of p53 signaling [64].A possible
427 explanation for these observations is that cell cycle-arrested TMZ-treated HF2927 CSCs may
428 have undergone apoptosis to a greater extent at the time point analyzed, as they demonstrated
429 increased sensitivity to TMZ treatment (Fig 5B). Furthermore, genes coding for proteins involved
430 in EMT, including the master regulator twist family bHLH transcription factor 1 (*TWIST1*), were
431 upregulated in response to TMZ exclusively in HF2927 SDCs, which could contribute to the
432 increased resistance of the differentiated cells.

433 **Table 2. Genes upregulated in HF2927 cells in response to temozolomide.**

Validated p53 direct targets			Other
CSC & SDC	**CSC**	**SDC**	**CSC & SDC**
ABCA12	*ALDH1A3*	*APOBEC3C*	*ABCA1*
ACER2	*ASTN2*	*CATSPERG*	*ANK1*
BBC3	*CEL*	*CES2*	*APLP1*
CDKN1A	*CLCA2*	*CGB7*	*BDNF*
COL7A1	*DRAM1*	*DDB2*	*CARNS1*
CPE	*EDA2R*	*EML2*	*F11R*
DGKA	*FAM13C*	*GPX1*	*FOXI3*
EPS8L2	*HES2*	*IGFBP7*	*FST*
FDXR	*KLHDC7A*	*MR1*	*GALNT5*
GDF15	*LAPTM5*	*MYOF*	*GDNF*
KITLG	*LIF*	*NINJ1*	*HKDC1*
PLK3	*MAST4*	*NKAIN4*	*INPP5D*
SERPINE1	*MDM2*	*PARD6G*	*IP6K3*
SPATA18	*NEFL*	*PGF*	*KIAA1217*
SULF2	*PDE4C*	*PHLDA3*	*KISS1R*
TP53I3	*PLCL2*	*PIDD1*	*LYNX1*
TRIM22	*PRDM1*	*PLXNB2*	*MARCH11*
WDR63	*RGS16*	*PRKX*	*MUC19*
	RRM2B	*RGMA*	*NECTIN4*
	SESN1	*RRAD*	*NEURL1*
	SYTL1	*SCN2A*	*NR5A1*
	TP53INP1	*SCN4B*	*NTN1*
	VWCE	*SESN2*	*OASL*
		TNFRSF10C	*PDGFC*
		TSPAN11	*PROCR*
		UNC5B	*SLC52A1*
			SMIM10L2A
			STC2
			TMEM80

434

435 Ionizing radiation can damage molecules directly, exerting most of its toxicity to cancer
436 cells through DNA double strand breaks (DSBs), and indirectly through the generation of free
437 radicals. The complex cellular responses leading to cell cycle arrest, apoptosis, DNA repair and
438 other processes occur over time [65]. The relative sensitivity of glioblastoma cells to RT varied
439 according to tumor of origin but not according to differentiation status under the experimental
440 parameters employed here (Fig 6A). Furthermore, pre-implantation treatment of CSCs with 4Gy

441 led to delayed xenograft tumor growth for all models (Fig 6B). To integrate these observations
442 with cellular responses, CSCs and SDCs were treated in triplicates with 4 Gy radiation dose or
443 mock radiation control, followed by incubation in the respective growth media for 5 days prior to
444 RNA isolation and sequencing. Under these conditions, few transcripts were altered in response
445 to RT in HF2303 (Fig 8B), consistent with the resistance to 4 Gy dose observed for both SDCs
446 and CSCs (Fig 6A). The only transcripts commonly upregulated in HF2303 CSCs and SDCs in
447 response to RT were phospholipase C eta 2 (*PLCH2*) and *SNORD3D* (Fig 8B). Interestingly, 50
448 of the pseudogenes involved in negative regulation of the execution phase of apoptosis, which
449 were downregulated in response to differentiation of CSCs into SDCs (Fig 7), were also
450 downregulated in RT-treated HF2303 CSCs (Fig 8B,C). Compared to TMZ treatment, fewer IFN
451 response genes were upregulated in RT treated cells, including *MX1* which was upregulated in
452 both CSC lines, and *OAS2*, *HERC6*, *IFI44L* and *HLA-E* in HF2927 CSCs (Table 1, Fig 8B). In
453 contrast to the response to TMZ, where the cells were analyzed after 4 days of continuous
454 treatment (Fig 8A), p53-mediated signaling in HF2927 was more attenuated 5 days after RT, as
455 expected (Fig 8B). Few p53 transcriptional targets remained elevated in irradiated HF2927 cells,
456 such as BCL2 Binding Component 3 (*BBC3 / PUMA*), a pro-apoptotic BCL-2 family member, while
457 expression of several others, including *MDM2*, were not altered at the 5-day timepoint (Fig 8B,D).
458 *CDKN1A*/p21, the main effector of p53 mediated cell cycle arrest significantly upregulated in
459 response to TMZ (Fig 8A), was elevated to a lesser degree in response to RT, below the statistical
460 threshold employed to determine DEGs (Fig 8D). However, sustained downregulation of cell cycle
461 genes downstream of p53 activation was observed for RT-treated HF2927 CSCs and SDCs (Fig
462 8B). Indeed, 53 out of the 56 transcripts commonly downregulated in HF2927 CSC and SDCs in
463 response to RT are transcriptional targets of the DREAM (dimerization partner, RB-like, E2F and
464 multivulval class B) repressive complex [66] (Table 3). Among these targets, forkhead box M1
465 (*FOXM1*), a transcriptional activator of cell cycle genes, especially those involved in G2 and M
466 phases [67], along with its transcriptional targets, including Polo-like kinase 1 (*PLK1*) which

467 phosphorylates and activates FOXM1 in a positive feed-back loop [68], were downregulated
468 exclusively in RT-treated cells at the analyzed time point (Fig. 8B,D). Furthermore, DNA damage
469 response and double strand break repair genes were downregulated in response to RT
470 predominantly in HF2927 CSCs (Fig 8B), indicating that these cells would be sensitized to
471 subsequent DNA damaging interventions.

472 **Table 3. Genes downregulated in HF2927 CSC and SDC in response to radiation.**

RT CSC/SDC	RT CSC/SDC & TMZ SDC	RT CSC/SDC & TMZ CSC/SDC
AURKB (*)	*ASPM (*)*	*CDC20 (*)*
BIRC5 (*)	*AURKA (*)*	*KIF20A (*)*
CCNA2 (*)	*BUB1 (*)*	
CCNB2 (*)	*BUB1B (*)*	
CDCA2 (*)	*CCNB1 (*)*	
DEPDC1 (*)	*CDCA8 (*)*	
ESPL1 (*)	*CENPE (*)*	
FOXM1 (*)	*CEP55 (*)*	
GTSE1 (*)	*DLGAP5 (*)*	
HIST1H1B (*)	*GAS2L3 (*)*	
HJURP (*)	*HIST1H2AB (*)*	
HMGB2 (*)	*HIST1H2AJ (*)*	
HMMR (*)	*HIST1H2AL (*)*	
IQGAP3 (*)	*HIST1H2BB*	
KIF15 (*)	*HIST1H2BO (*)*	
KIF23 (*)	*HIST1H3F (*)*	
KIF2C (*)	*HIST1H3G (*)*	
MELK (*)	*KIF11 (*)*	
NEK2 (*)	*KIF14 (*)*	
NUSAP1 (*)	*KIFC1 (*)*	
PIMREG	*KNL1*	
PRC1 (*)	*MKI67 (*)*	
PTTG1 (*)	*NCAPH (*)*	
RRM2 (*)	*NUF2 (*)*	
TROAP (*)	*PBK (*)*	
UBE2C (*)	*PLK1 (*)*	
	TPX2 (*)	
	TTK (*)	
(*)Transcriptional target of the DREAM repressor complex		

473

DNA methylation alteration pattern in differentiation of CSCs

To verify the contribution of epigenetic regulation to the transcriptional responses reported above, we analyzed the global DNA methylation profile of control and treated HF2303 and HF2927 CSCs and SDCs in triplicates, using Infinium Human Methylation 450K BeadChip. Differences in DNA methylation distinguished the samples according to the tumor of origin (HF2303 vs HF2927), as shown in the t-distributed stochastic neighbor embedding (t-SNE) plot (Fig 9A). Analysis of the differentially methylated positions (DMPs) and regions (DMRs) between CSC and SDC for each of these models identified 892 DMP and 12 DMRs for HF2303, and 27,431 DMP and 2 DMRs for HF2927 (S4 Table). Similar to the significant overlap in DEGs associated with CSC differentiation between the two cell lines (Fig 7B, D, Fig 9B), we identified 384 DMPs common to both lines (Fig 9B, S4 Table), with a pattern of decreased b-values in SDCs relative to CSCs in HF2303, while HF2927 SDCs exhibited an increase in b-values. The intersection between genes mapped to the DMPs, at the transcription start sites or within CpG islands, and the genes differentially expressed between CSCs and SDCs were limited to 17 and 59 genes for HF2303 and HF2927, respectively. Among these genes, latent transforming growth factor beta binding protein 3 (*LTBP3*) was associated with DMPs and upregulation in SDC for both models (Fig 9B, S4 Table). Cholesterol homeostasis, hypoxia, growth factor binding, and ECM components were significantly represented in the 59 gene list from HF2927 (S4 Table). No significant DNA methylation changes were observed in the acute response to RT and TMZ treatment across both models and differentiation states (S4 Fig).

Discussion

Understanding the extent to which oncogenic signaling and biological pathways modulating CSC phenotype and adaptation to external stimuli - such as astrocytic differentiation cues or growth factor withdrawal - are influenced by diverse genomic abnormalities, or are conversely generalizable to all GBMs, is crucial for the design and interpretation of biological and

499 experimental therapeutical studies. For example, astrocytic differentiation of CSCs into SDCs
500 resulted in the activation of RTK and MAPK pathways in most GBM cells, consistent with a role
501 for MAPK in early astrocytic differentiation [69]. However, this activation was not observed for the
502 two models carrying ecDNA EGFR amplification (HF2927 and HF3016). On the other hand, BMP-
503 Smad pathway was prominently activated in all GBM models upon exposure to 2% and 10% FBS.
504 Activation of BMP-Smad was further supported by the observation that transcriptional targets of
505 r-Smad1/5/8 were upregulated in HF2303 and HF2927 SDCs. This is consistent with the use of
506 BMP4 to induce the differentiation of iPSC into astrocytes [30], with BMP signaling inducing
507 astrocytic differentiation of patient-derived oligodendroglioma cells [70], and with BMP ligands
508 being present in FBS [33]. We found that signaling promoting cell survival in untreated GBM cells
509 varies among the different models but not as much between CSCs and SDCs. For example,
510 hyperactivation of the PI3K/AKT/mTOR pathway, which promotes cell growth, proliferation and
511 survival, is a common feature of GBMs [71], was observed in both CSCs and SDCs for 7/8 GBM
512 models, with a noted decrease in activation upon withdrawal of growth factors, as expected. The
513 integrated analysis of targeted proteomics in multiple GBM models, distinct differentiation states
514 and treatment groups showed a complex co-activation and cross talk among oncogenic signaling
515 pathways, which greatly contributes to aberrant cancer cell growth, proliferation, survival, and
516 resistance to therapeutic interventions [24]. We show that culturing CSCs in media supplemented
517 with 10% FBS resulted in suppression of key oncogenic signaling in all 8 GBM models, providing
518 further evidence that this media is not conducive to preserving GBM molecular characteristics, as
519 previously reported [28, 47].

520 Earlier studies characterized GBM "CSCs" as a subpopulation of cells isolated from
521 dissociated tumors based on expression of certain markers (e.g., CD133), which were
522 subsequently cultured in neural stem cell media, while marker-negative cells were considered
523 non-CSCs, or "differentiated", and cultured in 10% FBS. Using this paradigm, these earlier
524 studies attributed GBM marker positive "CSCs" with increased DNA repair capacity and

525 corresponding resistance to RT, when compared to marker negative “non-CSCs”, e.g. [72]. In
526 contrast, here GBM CSC subpopulations are propagated through enrichment in selective
527 neurosphere media, a widely employed strategy [11, 20, 21], and differentiated GBM cells are
528 defined as the progeny from astrocytic differentiation of CSCs in 2% FBS (SDCs). In this context,
529 we report that sensitivity to clinically relevant doses of RT was unchanged between CSCs and
530 their differentiated SDCs progeny, while SDCs presented increased resistance to TMZ for all three
531 models tested, two representing unmethylated and one methylated MGMT promoter. We show
532 that baseline levels of MGMT protein are strongly correlated with the levels of NF-kB activation in
533 GBM cells, regardless of MGMT promoter methylation status, supporting previous reports that
534 NF-kB activation confers resistance to DNA-alkylating agents in part through regulation of MGMT
535 in glioma [7].

536 Transcriptional reprograming associated with the differentiation of CSCs into SDCs
537 revealed two commonly altered cellular functions in the GBM models analyzed. Cholesterol
538 biosynthesis was enriched in CSCs, with evidence for transcriptional activity of sterol regulatory
539 element binding proteins (SREBPs), in response to the lack of cholesterol in the serum-free
540 neurosphere media. Because GBM cells tend to uptake cholesterol from the brain
541 microenvironment [73] and cholesterol is a component of FBS, cholesterol biosynthesis was
542 downregulated in SDCs (2% FBS). ECM components, receptors and regulators were upregulated
543 in SDCs, resembling transcriptional regulation of ECM components in astrocytes [74], likely with
544 contribution of stimulatory attachment factors in FBS. The enrichment in ECM-receptor interaction
545 observed for SDCs is associated with treatment resistance GBMs [75], and could be a factor
546 contributing to the increased resistance of GBM SDCs to TMZ treatment. The retention of the
547 expression of key stemness signature genes in SDCs, including *SOX2* and several of its
548 transcriptional targets, highlights the role of these genes in the maintenance of developmental
549 plasticity in more differentiated GBM cells, as we previously reported [26]. Other aspects of the
550 transcriptional reprograming associated with differentiation of CSCs were model specific. We had

551 previously shown that NF1 mutant HF2303 CSCs, like its parental tumor, belongs to the
552 mesenchymal subclass and can recapitulate the biphasic phenotype associated with
553 gliosarcoma, a GBM morphological variant, in orthotopic mouse xenografts [26]. Here, we show
554 that CSC differentiation for this model resulted in enrichment of EMT signature, analogous to the
555 mesenchymal cell state in NF1-deficient GBM [12]. DNA methylation alterations associated with
556 CSC differentiation varied, with 30-fold more DMPs identified for HF2927 relative to HF2303, but
557 the intersect between the 2 lines was highly significant at CpG level, but not at DMR level. On the
558 other hand, under the experimental conditions employed in this study, we did not observe
559 significant changes in global DNA methylation in response to treatment. There is no consensus
560 in the occurrence and extent of changes in global DNA methylation patterns in response to RT or
561 TMZ treatment in cultured cells [76]. This is in part due to the variability in cell intrinsic factors,
562 such as cell type, genomic alterations, proliferation rate and cell cycle phase, as well as extrinsic
563 factors, including culture conditions, RT and TMZ dosage and schedule.

564 We observed that both genomics and cell developmental states impact GBM response to
565 TMZ and RT. The status of *TP53*, a key regulator of cellular response to DNA-damaging agents,
566 was not surprisingly a key determinant of the transcriptional response of the GBM models to TMZ
567 and RT. HF2927 carries wt TP53 while HF2303 carries TP53 G245S, a dominant negative
568 mutation which disrupts the structure of p53 DNA binding domain, impairing p53 transcriptional
569 activity [77]. Furthermore, wt p53 transcriptional activation was modulated by differentiation
570 status, most notably in TMZ treated cells. Downregulation of cell cycle genes by p53 in response
571 to DNA-damage, accomplished indirectly through the DREAM repressive complex [66], was
572 observed for wt p53 CSCs and SDCs in response to TMZ and RT. *FOXM1,* a transcriptional
573 activator of cell cycle genes overexpressed in various cancers [67], and a DREAM target [66],
574 was highly expressed in untreated HF2303 and HF2927 cells. Here we show that *FOXM1*, along
575 with its downstream signaling, were exclusively downregulated in HF2927 CSCs and SDCs 5
576 days after RT, although p53 target genes, including *CDKN1A*/p21 were no longer upregulated at

577 this timepoint, indicating the prolonged effect of cell cycle arrest through downregulation of cell
578 cycle genes, downstream of p53 activation, but we show these cells retained their tumorigenic
579 potential.

580 Our work provides further evidence for a role of IFN response in resistance of GBMs to
581 the standard of care. It is well stablished that accumulation of cytoplasmic ssDNA or dsDNA in
582 cancer cells following DNA damage activates cGMP-AMP synthase (cGAS)–stimulator of IFN
583 genes (STING) pathway, leading to the activation of type I IFN production and upregulation of
584 IFN-stimulated genes (ISGs) [78]. Conflicting roles for IFN response ISGs in malignancy and
585 resistance to treatment have been proposed. For example, ISGs can promote RT resistance
586 through suppression of IFN production, in a negative feedback mechanism [79], or sensitize p53-
587 deficient cells to chemotherapy [80]. Others have shown that STAT1 suppression in classical GBM
588 CSCs leads to chemo-resistance [81]. IRDS is a subset of ISGs induced by prolonged exposure
589 to low doses of type I IFN [82], and associated with RT resistance to radiation in various cancers
590 [57]. *OAS1,* a member of the IRDS [57] involved in resistance to DNA-alkylating therapy [83], is
591 also part of the IFN/STAT1 prognostic signature proposed for GBM proneural subtype [63].
592 Because IFN response is coordinated and typically presents a high degree of correlation in gene
593 expression, our analysis identified genes highly correlated with expression to *OAS1* in the TCGA
594 GBM dataset. Upregulation of these IFN responsive genes was overrepresented in response to
595 TMZ and RT treatment of GBM CSCs and SDCs. Differentiation of HF2303 CSCs was
596 characterized by upregulation of IFN response genes. This is consistent with reports that cancer
597 cell-intrinsic type I IFN signaling is inversely correlated to stemness in a pan-cancer study [84].
598 We did not observe this IFN activation in HF2927 SDCs cells, highlighting the heterogeneity of
599 responses of GBM CSCs to external stimuli. Our results highlight the importance of the IFN
600 pathway activation in modulating glioma response to the standard of care, warranting further
601 exploration as a therapeutic target and predictive biomarker.

602 # Conclusions

603 These results from the integrated analysis of treatment response and differentiation in bulk
604 patient-derived GBM cell populations, which reflect the cumulative dynamic alterations in CSC
605 and SDC sub-compartments, provide both validation of existing research and novel insights for
606 further in vivo investigation, considering the added complexity of interactions among neoplastic
607 cells in different states and the tumor microenvironment. Our findings have important implications
608 for pre-clinical studies, highlighting the need for caution when generalizing results related to the
609 differentiation of CSCs or their treatment sensitivity and molecular response across diverse GBM
610 models.

611

612 # Methods

613 ## Cell culture

614 Glioblastoma patient-derived cancer stem cell cultures were obtained from the live biobank
615 collection at the Hermelin Brain Tumor Center, Henry Ford Hospital (Detroit, MI). These cells were
616 derived from de-identified surgically resected glioblastoma specimens, collected with written
617 informed consent, under a protocol approved by the HFH Institutional Review Board as previously
618 described [85], in compliance with all relevant ethical regulations for research using human
619 specimens. Cells were cultured in serum-free neurosphere media consisting of Dulbecco's
620 Modified Eagle Medium (DMEM)/F12 media (Invitrogen), N2 supplement (Gibco) and 0.5 mg/ml
621 BSA, supplemented with growth factors 20 ng/ml EGF and 20 ng/ml bFGF (Peprotech) (NMGF),
622 to select for CSCs [85]. CSC cultures were passaged in vitro and used prior to achieving passage
623 20. Identity of CSC lines was confirmed by comparing genotype with the patient germline using
624 Short Tandem Repeat (STR) analysis. CSCs were dissociated and cultured for 2 weeks in three
625 different conditions: NM lacking growth factors, and NMGF supplemented with 2% or 10% FBS

626 (HyClone). Neural progenitor cells (NPCs) were derived from H9 human ESC, obtained from
627 WiCell (Madison WI) as described [86] and differentiated in NMGF supplemented in 2% FBS [87].
628

629 Reverse Phase Protein Arrays analysis

630 Cell lysates were obtained in triplicate for each cell line and growth conditions described (Fig 1B).
631 The levels of 66 proteins/post-translational modifications in the cell lysates were analyzed by
632 Reverse Phase Protein Arrays (RPPA) at the Mason's Center for Applied Proteomics and
633 Molecular Medicine (George Mason University), essentially as described previously [31, 32].
634 Statistical analyses of RPPA normalized values were conducted in the R statistical environment
635 (4.2.1). Heatmaps were generated by ComplexHeatmap package in R (2.12.1) [88]. Z-scores for
636 each protein and post-translational modification were calculated based on population mean and
637 standard deviation ($(x-\mu)/\sigma$). Fold-change was calculated using the gTools package (3.9.3) and
638 computed as follows: num/denom if num>denom, and as -denom/num otherwise. Dendrograms
639 were produced using Spearman correlation as the distance method.
640

641 Cell proliferation, radiation and temozolomide treatment

642 Cell proliferation*:* Cell proliferation curves were established by plating 1,000 cells/well into 96-well
643 plates in NMGF (CSCs) or NMGF supplemented with 2% FBS (SDCs) and measuring cell viability
644 after 1, 4, 6, 8, and 11 days in culture (n=5). Wells were supplemented with fresh media every 3-
645 4 days. Cell viability was measured using CellTiter-Glo Luminescent Cell Viability Assay
646 (Promega), relative light units (RLU) were measured in a BioTek Cytation 3 plate reader. Doubling
647 time (DT) was calculated using the formula $DT=(t1-t2)\ln 2 / \ln(RLU2/RLU1)$.
648 Temozolomide dose-response curves*:* CSCs and SDCs were plated in 96-well assay plates
649 (3,000 cells/well), in quintuplicates and treated with 10 to 400 mM temozolomide (Schering-
650 Plough) or DMSO control for 4 days. CellTiterGlo (Promega) was used to measure cell viability

651 and dose-response curves were generated by non-linear fitting, IC50 doses and area above the
652 curve (AAC) were calculated in GraphPad Prism (v.9.0).
653 Ionizing radiation treatment (RT): CSC and SDC cells were dissociated, irradiated with 0, 2 or 4
654 Gy using a 5000 Ci Cesium (Cs-137) irradiator, and plated in triplicate at density of 3,000 cells/well
655 in 96-well assay plates in the respective growth media and incubated under standard conditions
656 for 5 days. Cell viability was assayed with CellTiter Glo (Promega). Surviving fractions at the two
657 radiation doses were calculated and compared.
658 Tumorigenic potential of irradiated cells: Mouse experiments were performed under an approved
659 Henry Ford Health Institutional Animal Care and Use Committee protocol (IACUC #1449) by
660 properly trained personnel. Single cell suspensions of glioblastoma CSCs constitutively
661 expressing firefly luciferase were irradiated with 0 (mock control) or 4Gy, as described above.
662 Immediately following radiation or control treatment, $2x10^5$ cells/mouse were implanted
663 intracranially in female NCRNU-M athymic nude mice (Taconic Farms), under anesthesia via
664 ketamine/xylazine intraperitoneal injection, as described in detail [89]. To compare survival
665 curves between mice implanted with CSCs treated with 0 Gy versus 4 Gy RT for each model, the
666 required sample size was calculated using PASS Sample Size Software. The calculation was
667 based on a one-tailed log-rank test with an alpha level of 0.10. With a sample size of 6 per group,
668 there is 81% power to detect a difference in survival probabilities of 95% versus 5%. To account
669 for possible losses, a total of 42 mice were used, n=7/group except for HF2303 for which n=6
670 mice were used for control and n=8 for irradiated CSCs. Following surgery to implant CSCs, mice
671 were kept warm using a heating pad until they regained consciousness, returned to the cages
672 and for 48h observed every 3h for any signs of distress, in which case buprenorphine can be
673 administered. Subsequently, mice continued to be monitored daily and were weighted 3 times a
674 week by a technician blinded to the experimental groups. Tumor growth was monitored by
675 noninvasive bioluminescence imaging using IVIS Spectrum In Vivo Imaging System (Caliper Life
676 Sciences) once a week. The primary endpoint of this study is symptom-free survival, and no mice

677 were excluded from the study. Within 6 hours after the observation of any symptoms associated
678 with tumor burden, which happened within 275 days post-implant, all 42 mice were euthanized
679 by >5% isoflurane overdose, and after no signs of palpebral reflexes and breathing were
680 observed, mice were decapitated as a second assurance of death. The symptoms included weight
681 loss greater than 20% of body mass, cranial protrusion, sickness, weakening, inactivity, anorexia,
682 hunched posture, sunken eyes, ruffled coat, abnormal head tilt, seizures, or ataxia.
683 Sublethal temozolomide and radiation treatment for total RNA and genomic DNA isolation:
684 *Temozolomide*: GBM CSCs or SDCs growing in their respective media were treated in triplicate
685 with the respective TMZ IC40 concentrations or control DMSO for 4 days. *Radiation*: Cells were
686 treated in triplicate with ionizing radiation (4Gy) or mock radiation control (0Gy) and cultured for
687 5 days. For all treatment groups, cells were harvested, total RNA isolated using RNeasy Mini Kit
688 (Qiagen) and used for RNA sequencing. Genomic DNA was isolated using QIAamp DNA kit
689 (Qiagen) and used for DNA methylation profiling.
690

691 # RNA Sequencing

692 RNA quality assessment was performed using the Agilent RNA ScreenTape on the Agilent 2200
693 TapeStation. Library for RNA sequencing was prepared using TruSeq Stranded Total RNA LT
694 (Illumina). 100 bps paired-end libraries were sequenced on the Illumina HiSeq 2500 following
695 cBot clustering. Prior to alignment the sequencing adaptors were trimmed using FASTQ Toolkit
696 v1.0 on Illumina's BaseSpace portal. FastQC was used to generate quality metrics for assessment
697 of FASTQ files [90]. RNA seq reads were aligned using TopHat v2.1.0 using default alignment
698 parameters and GRCh38 reference genome [91, 92]. After alignment, the mapped reads were
699 further filtered by mappability score (MAPQ ≥ 10) and sorted by genomic position of the reads
700 using samtools-0.1.19 [93]. PCR duplicate reads were processed and removed using rmdup
701 function (options -S) in samtools. The cleaned BAM files were further analyzed using Integrative

702 Genome Viewer (http://software.broadinstitute.org/software/igv/), processed with R function
703 "FeatureCount" to quantify reads on various RNA types from GencodeV28 annotation. Differential
704 gene expression analysis was performed using the non-parametric algorithm "NOISeq" in R **[94]**,
705 with q = 0.8 and fold change >2 or <0.5 thresholds on TMM normalized data for treated vs. control
706 comparisons, and q = 0.8 on RPKM normalized data for long term transcriptome changes in
707 untreated SDCs vs CSCs. Gene set enrichment tests for differentially expressed gene lists were
708 performed using Metascape 3.5, and adjusted p-value (q) < 0.05 [95].
709

710 DNA methylation analysis

711 Genomic DNA was analyzed using Infinium Human Methylation 450K BeadChip system
712 (Illumina), as described [86]. Raw methylation data was pre-processed for dye-bias normalization,
713 detection p-value was calculated by comparing the signal intensity difference between array
714 probes and a set of negative control probes on the array; probes with p-value greater than 0.01
715 filtered out. Beta values were calculated from pre-processed raw data using methylumi
716 Bioconductor package in R [96]. Probes mapping to known SNPs and sex chromosomes were
717 filtered out of dataset as recommended by Zhou et al. [97]. Beta values were corrected for batch
718 effect using ComBat function within sva R package [98, 99]. Probes were aligned to hg38 and
719 annotated using Illumina methylation 450k manifest [100]. Differentially methylated positions
720 between experimental groups (n=3/group) were determined using champ.DMP function, and to
721 determine differentially methylated regions we used the champ.DMR with Bumphunter method
722 from the ChAMP package in ChAMPs R package [101] with raw p-values < 0.05, and adjusted p-
723 value < 0.1. DMPs were annotated to genes using illuminaHg19 annotation employed by the
724 ChAMPs package in R. Analyses to determine the intersect of DMPs, the genes mapped to DMPs
725 and DEGs, within and between models, were carried out using GeneOverlap (version 1.34.0).
726

727 ## Cellular oxygen consumption rate

728 Cellular oxygen consumption rate (OCR) was measured using a Seahorse XF Cell Mito Stress
729 Test in a XFe24 Bioanalyzer (Agilent). Cells were plated at a concentration of 30,000 (HF2303)
730 or 40,000 (HF2927) per well on poly-ornithine hydrobromide (Sigma # 4957) coated plates in
731 NMGF media (CSC) or 2%FBS media (SDC) and treated for 4 days with DMSO or TMZ IC40
732 concentrations, prior to basal oxygen consumption measurements, performed according to the
733 manufacturer's instructions.
734

735 ## Statistical analysis

736 Statistical analyses were performed using GraphPad Prism (v. 9.00) or R and are described in
737 the results section for each experiment. Tumor growth in mouse PDX was evaluated by Kaplan-
738 Meier survival curves, compared by the log-rank test with $p<0.05$ considered significant.
739

740 # Data availability

741 The data discussed in this publication have been deposited in NCBI's Gene Expression Omnibus
742 [102] and are accessible through GEO Series accession number GSE249637.
743

744 # Funding

745 This work was supported by Department of Defense Idea award CA180174 (ACD) and the
746 Demchik Family Fund for Glioma Patient-Derived Avatar Models (ACD). ON received support
747 from NIH F31 CA250450-01, and AB was supported by NIH T32 CA009531 training fellowship
748 (Wayne State University).
749

750 # Competing Interests

751 The authors declare no competing interests.

752

753 # Acknowledgments

754 We thank Kristyn Quenneville and Dr. Nouman Mughal for their assistance with reviewing and
755 editing the manuscript.

756

757 # Author contributions

758 A.C.D. and D.R. conceived the study. K.B., Y.M., S.I., L.H., and A.B. performed cell culture,
759 treatment response, and prepared cell lysate, DNA and RNA for profiling. C.M. and E.F.P.
760 generated the RPPA data and performed initial analysis at Mason's Center for Applied Proteomics
761 and Molecular Medicine (CAPMM). AB performed RPPA data analysis. S.B. performed the
762 radiation experiments. KG and DR performed the RNA sequencing and DNA Methylation at the
763 Wayne State University Genomics Core. ID, LP and ON performed the RNAseq bioinformatics
764 analysis. OD, TS and HN performed the DNA methylation bioinformatics analysis. N.P. and S.A.
765 performed the OCR measurements. A.C.D., A.B. and O.N wrote the manuscript with input from
766 co-authors.

767

768

References

1. Louis DN, Perry A, Wesseling P, Brat DJ, Cree IA, Figarella-Branger D, et al. The 2021 WHO Classification of Tumors of the Central Nervous System: a summary. Neuro-oncology. 2021;23(8):1231-51. Epub 2021/06/30. doi: 10.1093/neuonc/noab106. PubMed PMID: 34185076; PubMed Central PMCID: PMCPMC8328013.
2. Marko NF, Weil RJ, Schroeder JL, Lang FF, Suki D, Sawaya RE. Extent of resection of glioblastoma revisited: personalized survival modeling facilitates more accurate survival prediction and supports a maximum-safe-resection approach to surgery. Journal of clinical oncology : official journal of the American Society of Clinical Oncology. 2014;32(8):774-82. Epub 20140210. doi: 10.1200/JCO.2013.51.8886. PubMed PMID: 24516010; PubMed Central PMCID: PMCPMC4876349.
3. Stupp R, Mason WP, van den Bent MJ, Weller M, Fisher B, Taphoorn MJ, et al. Radiotherapy plus concomitant and adjuvant temozolomide for glioblastoma. The New England journal of medicine. 2005;352(10):987-96. doi: 10.1056/NEJMoa043330. PubMed PMID: 15758009.
4. Marenco-Hillembrand L, Wijesekera O, Suarez-Meade P, Mampre D, Jackson C, Peterson J, et al. Trends in glioblastoma: outcomes over time and type of intervention: a systematic evidence based analysis. Journal of neuro-oncology. 2020;147(2):297-307. Epub 2020/03/12. doi: 10.1007/s11060-020-03451-6. PubMed PMID: 32157552.
5. Hegi ME, Diserens A-C, Gorlia T, Hamou M-F, de Tribolet N, Weller M, et al. MGMT Gene Silencing and Benefit from Temozolomide in Glioblastoma. The New England journal of medicine. 2005;352(10):997-1003.
6. Chen X, Zhang M, Gan H, Wang H, Lee JH, Fang D, et al. A novel enhancer regulates MGMT expression and promotes temozolomide resistance in glioblastoma. Nat Commun. 2018;9(1):2949. Epub 20180727. doi: 10.1038/s41467-018-05373-4. PubMed PMID: 30054476; PubMed Central PMCID: PMCPMC6063898.
7. Lavon I, Fuchs D, Zrihan D, Efroni G, Zelikovitch B, Fellig Y, Siegal T. Novel mechanism whereby nuclear factor kappaB mediates DNA damage repair through regulation of O(6)-methylguanine-DNA-methyltransferase. Cancer Res. 2007;67(18):8952-9. doi: 10.1158/0008-5472.CAN-06-3820. PubMed PMID: 17875738.
8. Sanchez-Vega F, Mina M, Armenia J, Chatila WK, Luna A, La KC, et al. Oncogenic Signaling Pathways in The Cancer Genome Atlas. Cell. 2018;173(2):321-37. e10.
9. Olson JJ, Nayak L, Ormond DR, Wen PY, Kalkanis SN, Ryken TC. The role of targeted therapies in the management of progressive glioblastoma: a systematic review and evidence-based clinical practice guideline. Journal of neuro-oncology. 2014;118:557-99.
10. Johnson BE, Mazor T, Hong C, Barnes M, Aihara K, McLean CY, et al. Mutational analysis reveals the origin and therapy-driven evolution of recurrent glioma. Science. 2014;343(6167):189-93. Epub 2013/12/18. doi: 10.1126/science.1239947. PubMed PMID: 24336570; PubMed Central PMCID: PMCPMC3998672.
11. deCarvalho AC, Kim H, Poisson LM, Winn ME, Mueller C, Cherba D, et al. Discordant inheritance of chromosomal and extrachromosomal DNA elements contributes to dynamic disease evolution in glioblastoma. Nat Genet. 2018;50(5):708-17.

Epub April 23. doi: 10.1038/s41588-018-0105-0. PubMed PMID: 29686388; PubMed Central PMCID: PMCPMC5934307.
12. Neftel C, Laffy J, Filbin MG, Hara T, Shore ME, Rahme GJ, et al. An Integrative Model of Cellular States, Plasticity, and Genetics for Glioblastoma. Cell. 2019;178(4):835-49 e21. Epub 20190718. doi: 10.1016/j.cell.2019.06.024. PubMed PMID: 31327527; PubMed Central PMCID: PMCPMC6703186.
13. Yabo YA, Niclou SP, Golebiewska A. Cancer cell heterogeneity and plasticity: A paradigm shift in glioblastoma. Neuro-oncology. 2022;24(5):669-82. doi: 10.1093/neuonc/noab269. PubMed PMID: 34932099; PubMed Central PMCID: PMCPMC9071273.
14. Reinartz R, Wang S, Kebir S, Silver DJ, Wieland A, Zheng T, et al. Functional Subclone Profiling for Prediction of Treatment-Induced Intratumor Population Shifts and Discovery of Rational Drug Combinations in Human Glioblastoma. Clin Cancer Res. 2017;23(2):562-74. Epub 20160812. doi: 10.1158/1078-0432.CCR-15-2089. PubMed PMID: 27521447; PubMed Central PMCID: PMCPMC5241221.
15. Suvà ML, Rheinbay E, Gillespie SM, Patel AP, Wakimoto H, Rabkin SD, et al. Reconstructing and reprogramming the tumor-propagating potential of glioblastoma stem-like cells. Cell. 2014;157(3):580-94.
16. Galli R, Binda E, Orfanelli U, Cipelletti B, Gritti A, De Vitis S, et al. Isolation and characterization of tumorigenic, stem-like neural precursors from human glioblastoma. Cancer Res. 2004;64(19):7011-21. PubMed PMID: 15466194.
17. Vescovi AL, Galli R, Reynolds BA. Brain tumour stem cells. Nat Rev Cancer. 2006;6(6):425-36. PubMed PMID: 16723989.
18. Ignatova TN, Kukekov VG, Laywell ED, Suslov ON, Vrionis FD, Steindler DA. Human cortical glial tumors contain neural stem-like cells expressing astroglial and neuronal markers in vitro. Glia. 2002;39(3):193-206. PubMed PMID: 12203386.
19. Hemmati HD, Nakano I, Lazareff JA, Masterman-Smith M, Geschwind DH, Bronner-Fraser M, Kornblum HI. Cancerous stem cells can arise from pediatric brain tumors. Proc Natl Acad Sci U S A. 2003;100(25):15178-83. PubMed PMID: 14645703.
20. Shen Y, Grisdale CJ, Islam SA, Bose P, Lever J, Zhao EY, et al. Comprehensive genomic profiling of glioblastoma tumors, BTICs, and xenografts reveals stability and adaptation to growth environments. Proc Natl Acad Sci U S A. 2019;116(38):19098-108. Epub 2019/09/01. doi: 10.1073/pnas.1813495116. PubMed PMID: 31471491; PubMed Central PMCID: PMCPMC6754609.
21. Woo XY, Giordano J, Srivastava A, Zhao ZM, Lloyd MW, de Bruijn R, et al. Conservation of copy number profiles during engraftment and passaging of patient-derived cancer xenografts. Nat Genet. 2021;53(1):86-99. Epub 20210107. doi: 10.1038/s41588-020-00750-6. PubMed PMID: 33414553; PubMed Central PMCID: PMCPMC7808565.
22. Quartararo CE, Reznik E, deCarvalho AC, Mikkelsen T, Stockwell BR. High-Throughput Screening of Patient-Derived Cultures Reveals Potential for Precision Medicine in Glioblastoma. ACS medicinal chemistry letters. 2015;6(8):948-52. doi: 10.1021/acsmedchemlett.5b00128. PubMed PMID: 26288699; PubMed Central PMCID: PMC4538440.
23. Brennan CW, Verhaak RG, McKenna A, Campos B, Noushmehr H, Salama SR, et al. The somatic genomic landscape of glioblastoma. Cell. 2013;155(2):462-77. Epub

858 2013/10/15. doi: 10.1016/j.cell.2013.09.034. PubMed PMID: 24120142; PubMed Central
859 PMCID: PMCPMC3910500.
860 24. Mendoza MC, Er EE, Blenis J. The Ras-ERK and PI3K-mTOR pathways: cross-
861 talk and compensation. Trends Biochem Sci. 2011;36(6):320-8. Epub 20110430. doi:
862 10.1016/j.tibs.2011.03.006. PubMed PMID: 21531565; PubMed Central PMCID:
863 PMCPMC3112285.
864 25. Ye LF, Reznik E, Korn JM, Lin F, Yang G, Malesky K, et al. Patient-derived
865 glioblastoma cultures as a tool for small-molecule drug discovery. Oncotarget.
866 2020;11(4):443-51. Epub 2020/02/18. doi: 10.18632/oncotarget.27457. PubMed PMID:
867 32064048; PubMed Central PMCID: PMCPMC6996910.
868 26. Berezovsky AD, Poisson LM, Cherba D, Webb CP, Transou AD, Lemke NW, et al.
869 Sox2 promotes malignancy in glioblastoma by regulating plasticity and astrocytic
870 differentiation. Neoplasia. 2014;16(3):193-206 e25. Epub 2014/04/15. doi:
871 10.1016/j.neo.2014.03.006. PubMed PMID: 24726753.
872 27. Zheng X, Baker H, Hancock WS, Fawaz F, McCaman M, Pungor E, Jr. Proteomic
873 analysis for the assessment of different lots of fetal bovine serum as a raw material for
874 cell culture. Part IV. Application of proteomics to the manufacture of biological drugs.
875 Biotechnol Prog. 2006;22(5):1294-300. doi: 10.1021/bp060121o. PubMed PMID:
876 17022666.
877 28. Lee J, Kotliarova S, Kotliarov Y, Li A, Su Q, Donin NM, et al. Tumor stem cells
878 derived from glioblastomas cultured in bFGF and EGF more closely mirror the phenotype
879 and genotype of primary tumors than do serum-cultured cell lines. Cancer cell.
880 2006;9(5):391-403. PubMed PMID: 16697959.
881 29. Shaltouki A, Peng J, Liu Q, Rao MS, Zeng X. Efficient generation of astrocytes
882 from human pluripotent stem cells in defined conditions. Stem Cells. 2013;31(5):941-52.
883 doi: 10.1002/stem.1334. PubMed PMID: 23341249.
884 30. Tcw J, Wang M, Pimenova AA, Bowles KR, Hartley BJ, Lacin E, et al. An Efficient
885 Platform for Astrocyte Differentiation from Human Induced Pluripotent Stem Cells. Stem
886 cell reports. 2017;9(2):600-14. Epub 20170727. doi: 10.1016/j.stemcr.2017.06.018.
887 PubMed PMID: 28757165; PubMed Central PMCID: PMCPMC5550034.
888 31. Mueller C, deCarvalho AC, Mikkelsen T, Lehman NL, Calvert V, Espina V, et al.
889 Glioblastoma cell enrichment is critical for analysis of phosphorylated drug targets and
890 proteomic-genomic correlations. Cancer Res. 2014;74(3):818-28. Epub 2013/12/19. doi:
891 10.1158/0008-5472.CAN-13-2172. PubMed PMID: 24346432.
892 32. Pin E, Federici G, Petricoin EF, 3rd. Preparation and use of reverse protein
893 microarrays. Current protocols in protein science / editorial board, John E Coligan [et al].
894 2014;75:Unit 27 7. doi: 10.1002/0471140864.ps2707s75. PubMed PMID: 24510676.
895 33. Kodaira K, Imada M, Goto M, Tomoyasu A, Fukuda T, Kamijo R, et al. Purification
896 and identification of a BMP-like factor from bovine serum. Biochem Biophys Res
897 Commun. 2006;345(3):1224-31. Epub 20060515. doi: 10.1016/j.bbrc.2006.05.045.
898 PubMed PMID: 16716261.
899 34. Yang G, Murashige DS, Humphrey SJ, James DE. A Positive Feedback Loop
900 between Akt and mTORC2 via SIN1 Phosphorylation. Cell reports. 2015;12(6):937-43.
901 Epub 20150730. doi: 10.1016/j.celrep.2015.07.016. PubMed PMID: 26235620.

35. Efeyan A, Sabatini DM. mTOR and cancer: many loops in one pathway. Curr Opin Cell Biol. 2010;22(2):169-76. Epub 20091127. doi: 10.1016/j.ceb.2009.10.007. PubMed PMID: 19945836; PubMed Central PMCID: PMCPMC2854285.
36. Copp J, Manning G, Hunter T. TORC-specific phosphorylation of mammalian target of rapamycin (mTOR): phospho-Ser2481 is a marker for intact mTOR signaling complex 2. Cancer Res. 2009;69(5):1821-7. Epub 20090224. doi: 10.1158/0008-5472.CAN-08-3014. PubMed PMID: 19244117; PubMed Central PMCID: PMCPMC2652681.
37. Boutouja F, Stiehm CM, Platta HW. mTOR: A Cellular Regulator Interface in Health and Disease. Cells. 2019;8(1). Epub 20190102. doi: 10.3390/cells8010018. PubMed PMID: 30609721; PubMed Central PMCID: PMCPMC6356367.
38. Ovens AJ, Scott JW, Langendorf CG, Kemp BE, Oakhill JS, Smiles WJ. Post-Translational Modifications of the Energy Guardian AMP-Activated Protein Kinase. Int J Mol Sci. 2021;22(3). Epub 20210127. doi: 10.3390/ijms22031229. PubMed PMID: 33513781; PubMed Central PMCID: PMCPMC7866021.
39. Dite TA, Ling NXY, Scott JW, Hoque A, Galic S, Parker BL, et al. The autophagy initiator ULK1 sensitizes AMPK to allosteric drugs. Nat Commun. 2017;8(1):571. Epub 20170918. doi: 10.1038/s41467-017-00628-y. PubMed PMID: 28924239; PubMed Central PMCID: PMCPMC5603566.
40. Cirotti C, Contadini C, Barila D. SRC Kinase in Glioblastoma News from an Old Acquaintance. Cancers. 2020;12(6). Epub 20200612. doi: 10.3390/cancers12061558. PubMed PMID: 32545574; PubMed Central PMCID: PMCPMC7352599.
41. Okada M. Regulation of the SRC family kinases by Csk. Int J Biol Sci. 2012;8(10):1385-97. Epub 20121101. doi: 10.7150/ijbs.5141. PubMed PMID: 23139636; PubMed Central PMCID: PMCPMC3492796.
42. Irtegun S, Wood RJ, Ormsby AR, Mulhern TD, Hatters DM. Tyrosine 416 is phosphorylated in the closed, repressed conformation of c-Src. PloS one. 2013;8(7):e71035. Epub 20130726. doi: 10.1371/journal.pone.0071035. PubMed PMID: 23923048; PubMed Central PMCID: PMCPMC3724807.
43. Metz HE, Houghton AM. Insulin receptor substrate regulation of phosphoinositide 3-kinase. Clin Cancer Res. 2011;17(2):206-11. Epub 20101021. doi: 10.1158/1078-0432.CCR-10-0434. PubMed PMID: 20966354.
44. Li J, Choi E, Yu H, Bai XC. Structural basis of the activation of type 1 insulin-like growth factor receptor. Nat Commun. 2019;10(1):4567. Epub 20191008. doi: 10.1038/s41467-019-12564-0. PubMed PMID: 31594955; PubMed Central PMCID: PMCPMC6783537.
45. Shah OJ, Hunter T. Turnover of the active fraction of IRS1 involves raptor-mTOR- and S6K1-dependent serine phosphorylation in cell culture models of tuberous sclerosis. Mol Cell Biol. 2006;26(17):6425-34. doi: 10.1128/MCB.01254-05. PubMed PMID: 16914728; PubMed Central PMCID: PMCPMC1592824.
46. Rena G, Prescott AR, Guo S, Cohen P, Unterman TG. Roles of the forkhead in rhabdomyosarcoma (FKHR) phosphorylation sites in regulating 14-3-3 binding, transactivation and nuclear targetting. Biochem J. 2001;354(Pt 3):605-12. doi: 10.1042/0264-6021:3540605. PubMed PMID: 11237865; PubMed Central PMCID: PMCPMC1221692.
47. Li A, Walling J, Kotliarov Y, Center A, Steed ME, Ahn SJ, et al. Genomic changes and gene expression profiles reveal that established glioma cell lines are poorly

948 representative of primary human gliomas. Mol Cancer Res. 2008;6(1):21-30. PubMed
949 PMID: 18184972.
950 48. Mighell TL, Evans-Dutson S, O'Roak BJ. A Saturation Mutagenesis Approach to
951 Understanding PTEN Lipid Phosphatase Activity and Genotype-Phenotype
952 Relationships. Am J Hum Genet. 2018;102(5):943-55. Epub 20180426. doi:
953 10.1016/j.ajhg.2018.03.018. PubMed PMID: 29706350; PubMed Central PMCID:
954 PMCPMC5986715.
955 49. Vazquez F, Ramaswamy S, Nakamura N, Sellers WR. Phosphorylation of the
956 PTEN tail regulates protein stability and function. Mol Cell Biol. 2000;20(14):5010-8. doi:
957 10.1128/MCB.20.14.5010-5018.2000. PubMed PMID: 10866658; PubMed Central
958 PMCID: PMCPMC85951.
959 50. Rubio-Camacho M, Encinar JA, Martinez-Tome MJ, Esquembre R, Mateo CR. The
960 Interaction of Temozolomide with Blood Components Suggests the Potential Use of
961 Human Serum Albumin as a Biomimetic Carrier for the Drug. Biomolecules. 2020;10(7).
962 Epub 20200709. doi: 10.3390/biom10071015. PubMed PMID: 32659914; PubMed
963 Central PMCID: PMCPMC7408562.
964 51. Manem VS, Lambie M, Smith I, Smirnov P, Kofia V, Freeman M, et al. Modeling
965 Cellular Response in Large-Scale Radiogenomic Databases to Advance Precision
966 Radiotherapy. Cancer Res. 2019;79(24):6227-37. Epub 2019/09/29. doi: 10.1158/0008-
967 5472.CAN-19-0179. PubMed PMID: 31558563; PubMed Central PMCID:
968 PMCPMC8128135.
969 52. Sancho P, Barneda D, Heeschen C. Hallmarks of cancer stem cell metabolism. Br
970 J Cancer. 2016;114(12):1305-12. Epub 20160524. doi: 10.1038/bjc.2016.152. PubMed
971 PMID: 27219018; PubMed Central PMCID: PMCPMC4984474.
972 53. Yamatani Y, Nakai K. Comprehensive comparison of gene expression diversity
973 among a variety of human stem cells. NAR Genom Bioinform. 2022;4(4):lqac087. Epub
974 20221129. doi: 10.1093/nargab/lqac087. PubMed PMID: 36458020; PubMed Central
975 PMCID: PMCPMC9706419.
976 54. Bodzioch M, Lapicka-Bodzioch K, Zapala B, Kamysz W, Kiec-Wilk B, Dembinska-
977 Kiec A. Evidence for potential functionality of nuclearly-encoded humanin isoforms.
978 Genomics. 2009;94(4):247-56. Epub 20090527. doi: 10.1016/j.ygeno.2009.05.006.
979 PubMed PMID: 19477263.
980 55. Fischer M. Census and evaluation of p53 target genes. Oncogene.
981 2017;36(28):3943-56. Epub 20170313. doi: 10.1038/onc.2016.502. PubMed PMID:
982 28288132; PubMed Central PMCID: PMCPMC5511239.
983 56. Gimple RC, Kidwell RL, Kim LJY, Sun T, Gromovsky AD, Wu Q, et al. Glioma Stem
984 Cell-Specific Superenhancer Promotes Polyunsaturated Fatty-Acid Synthesis to Support
985 EGFR Signaling. Cancer discovery. 2019;9(9):1248-67. Epub 20190614. doi:
986 10.1158/2159-8290.CD-19-0061. PubMed PMID: 31201181; PubMed Central PMCID:
987 PMCPMC6785242.
988 57. Weichselbaum RR, Ishwaran H, Yoon T, Nuyten DS, Baker SW, Khodarev N, et al.
989 An interferon-related gene signature for DNA damage resistance is a predictive marker
990 for chemotherapy and radiation for breast cancer. Proc Natl Acad Sci U S A.
991 2008;105(47):18490-5. Epub 20081110. doi: 10.1073/pnas.0809242105. PubMed PMID:
992 19001271; PubMed Central PMCID: PMCPMC2587578.

58. Tanner SM, Austin JL, Leone G, Rush LJ, Plass C, Heinonen K, et al. BAALC, the human member of a novel mammalian neuroectoderm gene lineage, is implicated in hematopoiesis and acute leukemia. Proc Natl Acad Sci U S A. 2001;98(24):13901-6. Epub 2001/11/15. doi: 10.1073/pnas.241525498. PubMed PMID: 11707601; PubMed Central PMCID: PMC61139.
59. Ferrandez E, Gutierrez O, Segundo DS, Fernandez-Luna JL. NFkappaB activation in differentiating glioblastoma stem-like cells is promoted by hyaluronic acid signaling through TLR4. Sci Rep. 2018;8(1):6341. Epub 20180420. doi: 10.1038/s41598-018-24444-6. PubMed PMID: 29679017; PubMed Central PMCID: PMCPMC5910430.
60. Bochukova EG, Lawler K, Croizier S, Keogh JM, Patel N, Strohbehn G, et al. A Transcriptomic Signature of the Hypothalamic Response to Fasting and BDNF Deficiency in Prader-Willi Syndrome. Cell reports. 2018;22(13):3401-8. doi: 10.1016/j.celrep.2018.03.018. PubMed PMID: 29590610; PubMed Central PMCID: PMCPMC5896230.
61. Amsden H, Kourko O, Roth M, Gee K. Antiviral Activities of Interleukin-27: A Partner for Interferons? Front Immunol. 2022;13:902853. Epub 20220510. doi: 10.3389/fimmu.2022.902853. PubMed PMID: 35634328; PubMed Central PMCID: PMCPMC9134790.
62. Cerami E, Gao J, Dogrusoz U, Gross BE, Sumer SO, Aksoy BA, et al. The cBio cancer genomics portal: an open platform for exploring multidimensional cancer genomics data. Cancer discovery. 2012;2(5):401-4. Epub 2012/05/17. doi: 10.1158/2159-8290.CD-12-0095. PubMed PMID: 22588877.
63. Duarte CW, Willey CD, Zhi D, Cui X, Harris JJ, Vaughan LK, et al. Expression signature of IFN/STAT1 signaling genes predicts poor survival outcome in glioblastoma multiforme in a subtype-specific manner. PloS one. 2012;7(1):e29653. Epub 20120105. doi: 10.1371/journal.pone.0029653. PubMed PMID: 22242177; PubMed Central PMCID: PMCPMC3252343.
64. Engeland K. Cell cycle arrest through indirect transcriptional repression by p53: I have a DREAM. Cell Death Differ. 2018;25(1):114-32. Epub 20171110. doi: 10.1038/cdd.2017.172. PubMed PMID: 29125603; PubMed Central PMCID: PMCPMC5729532.
65. Baskar R, Dai J, Wenlong N, Yeo R, Yeoh KW. Biological response of cancer cells to radiation treatment. Front Mol Biosci. 2014;1:24. Epub 20141117. doi: 10.3389/fmolb.2014.00024. PubMed PMID: 25988165; PubMed Central PMCID: PMCPMC4429645.
66. Fischer M, Grossmann P, Padi M, DeCaprio JA. Integration of TP53, DREAM, MMB-FOXM1 and RB-E2F target gene analyses identifies cell cycle gene regulatory networks. Nucleic acids research. 2016;44(13):6070-86. Epub 20160608. doi: 10.1093/nar/gkw523. PubMed PMID: 27280975; PubMed Central PMCID: PMCPMC4994865.
67. Fischer M, Schade AE, Branigan TB, Muller GA, DeCaprio JA. Coordinating gene expression during the cell cycle. Trends Biochem Sci. 2022;47(12):1009-22. Epub 20220711. doi: 10.1016/j.tibs.2022.06.007. PubMed PMID: 35835684.
68. Marceau AH, Brison CM, Nerli S, Arsenault HE, McShan AC, Chen E, et al. An order-to-disorder structural switch activates the FoxM1 transcription factor. Elife. 2019;8.

1038 Epub 20190528. doi: 10.7554/eLife.46131. PubMed PMID: 31134895; PubMed Central
1039 PMCID: PMCPMC6538375.
1040 69. Rajan P, McKay RD. Multiple routes to astrocytic differentiation in the CNS. J
1041 Neurosci. 1998;18(10):3620-9. doi: 10.1523/JNEUROSCI.18-10-03620.1998. PubMed
1042 PMID: 9570793; PubMed Central PMCID: PMCPMC6793143.
1043 70. Srikanth M, Kim J, Das S, Kessler JA. BMP signaling induces astrocytic
1044 differentiation of clinically derived oligodendroglioma propagating cells. Mol Cancer Res.
1045 2014;12(2):283-94. Epub 20131122. doi: 10.1158/1541-7786.MCR-13-0349. PubMed
1046 PMID: 24269952; PubMed Central PMCID: PMCPMC4006982.
1047 71. Zhang Y, Kwok-Shing Ng P, Kucherlapati M, Chen F, Liu Y, Tsang YH, et al. A Pan-
1048 Cancer Proteogenomic Atlas of PI3K/AKT/mTOR Pathway Alterations. Cancer cell.
1049 2017;31(6):820-32 e3. Epub 20170518. doi: 10.1016/j.ccell.2017.04.013. PubMed PMID:
1050 28528867; PubMed Central PMCID: PMCPMC5502825.
1051 72. Bao S, Wu Q, McLendon RE, Hao Y, Shi Q, Hjelmeland AB, et al. Glioma stem
1052 cells promote radioresistance by preferential activation of the DNA damage response.
1053 Nature. 2006;444(7120):756-60. Epub 2006/10/20. doi: 10.1038/nature05236. PubMed
1054 PMID: 17051156.
1055 73. Villa GR, Hulce JJ, Zanca C, Bi J, Ikegami S, Cahill GL, et al. An LXR-Cholesterol
1056 Axis Creates a Metabolic Co-Dependency for Brain Cancers. Cancer cell.
1057 2016;30(5):683-93. Epub 20161013. doi: 10.1016/j.ccell.2016.09.008. PubMed PMID:
1058 27746144; PubMed Central PMCID: PMCPMC5479636.
1059 74. Wiese S, Karus M, Faissner A. Astrocytes as a source for extracellular matrix
1060 molecules and cytokines. Frontiers in pharmacology. 2012;3:120. Epub 20120626. doi:
1061 10.3389/fphar.2012.00120. PubMed PMID: 22740833; PubMed Central PMCID:
1062 PMCPMC3382726.
1063 75. Segerman A, Niklasson M, Haglund C, Bergstrom T, Jarvius M, Xie Y, et al. Clonal
1064 Variation in Drug and Radiation Response among Glioma-Initiating Cells Is Linked to
1065 Proneural-Mesenchymal Transition. Cell reports. 2016;17(11):2994-3009. doi:
1066 10.1016/j.celrep.2016.11.056. PubMed PMID: 27974212.
1067 76. Zielske SP. Epigenetic DNA methylation in radiation biology: on the field or on the
1068 sidelines? J Cell Biochem. 2015;116(2):212-7. doi: 10.1002/jcb.24959. PubMed PMID:
1069 25186310.
1070 77. Hanel W, Marchenko N, Xu S, Xiaofeng Yu S, Weng W, Moll U. Two hot spot
1071 mutant p53 mouse models display differential gain of function in tumorigenesis. Cell
1072 Death & Differentiation. 2013;20(7):898-909.
1073 78. Cheon H, Wang Y, Wightman SM, Jackson MW, Stark GR. How cancer cells make
1074 and respond to interferon-I. Trends in cancer. 2023;9(1):83-92.
1075 79. Widau RC, Parekh AD, Ranck MC, Golden DW, Kumar KA, Sood RF, et al. RIG-I–
1076 like receptor LGP2 protects tumor cells from ionizing radiation. Proceedings of the
1077 National Academy of Sciences. 2014;111(4):E484-E91.
1078 80. Leonova KI, Brodsky L, Lipchick B, Pal M, Novototskaya L, Chenchik AA, et al.
1079 p53 cooperates with DNA methylation and a suicidal interferon response to maintain
1080 epigenetic silencing of repeats and noncoding RNAs. Proceedings of the National
1081 Academy of Sciences. 2013;110(1):E89-E98.

1082 81. Zhan X, Guo S, Li Y, Ran H, Huang H, Mi L, et al. Glioma stem-like cells evade
1083 interferon suppression through MBD3/NuRD complex–mediated STAT1 downregulation.
1084 Journal of Experimental Medicine. 2020;217(5):e20191340.
1085 82. Khodarev NN, Beckett M, Labay E, Darga T, Roizman B, Weichselbaum RR.
1086 STAT1 is overexpressed in tumors selected for radioresistance and confers protection
1087 from radiation in transduced sensitive cells. Proceedings of the National Academy of
1088 Sciences. 2004;101(6):1714-9.
1089 83. Kondratova A, Cheon H, Dong B, Holvey-Bates EG, Hasipek M, Taran I, et al.
1090 Suppressing PARylation by 2',5'-oligoadenylate synthetase 1 inhibits DNA damage-
1091 induced cell death. EMBO J. 2020;39(20):e106593. doi: 10.15252/embj.2020106593.
1092 PubMed PMID: 33058249; PubMed Central PMCID: PMCPMC7560197.
1093 84. Miranda A, Hamilton PT, Zhang AW, Pattnaik S, Becht E, Mezheyeuski A, et al.
1094 Cancer stemness, intratumoral heterogeneity, and immune response across cancers.
1095 Proc Natl Acad Sci U S A. 2019;116(18):9020-9. Epub 20190417. doi:
1096 10.1073/pnas.1818210116. PubMed PMID: 30996127; PubMed Central PMCID:
1097 PMCPMC6500180.
1098 85. Hasselbach LA, Irtenkauf SM, Lemke NW, Nelson KK, Berezovsky AD, Carlton ET,
1099 et al. Optimization of High Grade Glioma Cell Culture from Surgical Specimens for Use
1100 in Clinically Relevant Animal Models and 3D Immunochemistry. J Vis Exp.
1101 2014;83:e51088. Epub 2014/01/17. doi: 10.3791/51088. PubMed PMID: 24429465.
1102 86. Senut MC, Sen A, Cingolani P, Shaik A, Land SJ, Ruden DM. Lead exposure
1103 disrupts global DNA methylation in human embryonic stem cells and alters their neuronal
1104 differentiation. Toxicol Sci. 2014;139(1):142-61. Epub 2014/02/13. doi:
1105 10.1093/toxsci/kfu028. PubMed PMID: 24519525; PubMed Central PMCID:
1106 PMCPMC4023291.
1107 87. Haidet-Phillips AM, Hester ME, Miranda CJ, Meyer K, Braun L, Frakes A, et al.
1108 Astrocytes from familial and sporadic ALS patients are toxic to motor neurons. Nat
1109 Biotechnol. 2011;29(9):824-8. Epub 2011/08/13. doi: 10.1038/nbt.1957. PubMed PMID:
1110 21832997; PubMed Central PMCID: PMCPMC3170425.
1111 88. Gu Z, Eils R, Schlesner M. Complex heatmaps reveal patterns and correlations in
1112 multidimensional genomic data. Bioinformatics. 2016;32(18):2847-9. Epub 20160520.
1113 doi: 10.1093/bioinformatics/btw313. PubMed PMID: 27207943.
1114 89. Irtenkauf SM, Sobiechowski S, Hasselbach LA, Nelson KK, Transou AD, Carlton
1115 ET, et al. Optimization of Glioblastoma Mouse Orthotopic Xenograft Models for
1116 Translational Research. Comparative medicine. 2017;67(4):300-14. Epub May 16. doi:
1117 no_doi/1494959945479. PubMed PMID: 28830577; PubMed Central PMCID:
1118 PMCPMC5557202.
1119 90. Andrews S. FastQC A Quality Control Tool for High Throughput Sequence Data.
1120 Available online at: http://www.bioinformatics.babraham.ac.uk/projects/fastqc2010.
1121 91. Kim D, Pertea G, Trapnell C, Pimentel H, Kelley R, Salzberg SL. TopHat2: accurate
1122 alignment of transcriptomes in the presence of insertions, deletions and gene fusions.
1123 Genome Biol. 2013;14(4):R36. Epub 2013/04/27. doi: 10.1186/gb-2013-14-4-r36.
1124 PubMed PMID: 23618408; PubMed Central PMCID: PMCPMC4053844.
1125 92. Trapnell C, Pachter L, Salzberg SL. TopHat: discovering splice junctions with RNA-
1126 Seq. Bioinformatics. 2009;25(9):1105-11. Epub 2009/03/18. doi:

10.1093/bioinformatics/btp120. PubMed PMID: 19289445; PubMed Central PMCID: PMCPMC2672628.
93. Li H, Handsaker B, Wysoker A, Fennell T, Ruan J, Homer N, et al. The Sequence Alignment/Map format and SAMtools. Bioinformatics. 2009;25(16):2078-9. Epub 2009/06/10. doi: 10.1093/bioinformatics/btp352. PubMed PMID: 19505943; PubMed Central PMCID: PMCPMC2723002.
94. Tarazona S, Furio-Tari P, Turra D, Pietro AD, Nueda MJ, Ferrer A, Conesa A. Data quality aware analysis of differential expression in RNA-seq with NOISeq R/Bioc package. Nucleic acids research. 2015;43(21):e140. Epub 2015/07/18. doi: 10.1093/nar/gkv711. PubMed PMID: 26184878; PubMed Central PMCID: PMCPMC4666377.
95. Zhou Y, Zhou B, Pache L, Chang M, Khodabakhshi AH, Tanaseichuk O, et al. Metascape provides a biologist-oriented resource for the analysis of systems-level datasets. Nat Commun. 2019;10(1):1523. Epub 2019/04/05. doi: 10.1038/s41467-019-09234-6. PubMed PMID: 30944313; PubMed Central PMCID: PMCPMC6447622.
96. Davis S, Du P, Bilke S, Triche Jr. T, Bootwalla M. methylumi: Handle Illumina methylation data. R package version 2.30.0. (DOI: 10.18129/B9.bioc.methylumi). 2019.
97. Zhou W, Laird PW, Shen H. Comprehensive characterization, annotation and innovative use of Infinium DNA methylation BeadChip probes. Nucleic acids research. 2017;45(4):e22. Epub 2016/12/08. doi: 10.1093/nar/gkw967. PubMed PMID: 27924034; PubMed Central PMCID: PMCPMC5389466.
98. Leek JT, Johnson WE, Parker HS, Fertig EJ, Jaffe AE, Storey JD, et al. sva: Surrogate Variable Analysis. R package version 3.32.1. 2019.
99. Johnson WE, Li C, Rabinovic A. Adjusting batch effects in microarray expression data using empirical Bayes methods. Biostatistics (Oxford, England). 2007;8(1):118-27. Epub 2006/04/25. doi: 10.1093/biostatistics/kxj037. PubMed PMID: 16632515.
100. Hansen KD, Aryee M. IlluminaHumanMethylation450kmanifest: Annotation for Illumina's 450k methylation arrays. R package version 0.4.0. (DOI: 10.18129/B9.bioc.IlluminaHumanMethylation450kmanifest). 2012.
101. Tian Y, Morris TJ, Webster AP, Yang Z, Beck S, Feber A, Teschendorff AE. ChAMP: updated methylation analysis pipeline for Illumina BeadChips. Bioinformatics. 2017;33(24):3982-4. doi: 10.1093/bioinformatics/btx513. PubMed PMID: 28961746; PubMed Central PMCID: PMCPMC5860089.
102. Clough E, Barrett T, Wilhite SE, Ledoux P, Evangelista C, Kim IF, et al. NCBI GEO: archive for gene expression and epigenomics data sets: 23-year update. Nucleic acids research. 2023. Epub 20231102. doi: 10.1093/nar/gkad965. PubMed PMID: 37933855.

Supporting information

S1_Fig. Alteration in glioblastoma cancer stem cell signaling in response to growth factors withdrawal and differentiation in 2% FBS. A) Box plot representing changes in the levels of 66 proteins/PTM in response to 14-days culture in the absence of growth factors (NM), or upon serum differentiation (2%FBS), relative to CSC culture conditions (NMGF), using mean values from triplicate RPPA measurements for each of the 8 models. Plot represents n=507 data points, after proteins/PTMs which were not detected under all three culture conditions were filtered out for each model.

1171 **S2_Fig. MGMT promoter methylation.** Heatmap representing β-values of 26 CpG sites mapping
1172 to MGMT promoter, for HF2303 and HF2927 CSC and SDCs in control, TMZ and RT treatment
1173 groups, in triplicate. Human astrocyte cell line was included as reference. The two probes widely
1174 employed in the clinic to determine MGMT promoter methylation status ("predictive probes")
1175 indicate MGMT promoter hypermethylation in HF2927 and unmethylated status in HF2303 and
1176 human astrocytes cells. Differentiation status and treatment did not alter promoter methylation
1177 levels for either GBM line.

1178 **S3_Fig. Alterations in cellular respiration in response to treatment.** A) Basal (B) and
1179 maximum (M) relative oxygen consumption rate (OCR) for CSCs and SDCs measured after a 4-
1180 day treatment with TMZ, or 4 days after treatment with one 4 Gy radiation dose. OCR values were
1181 normalized to CSC (left panel) and SDC (right panel) HF2303 basal levels (%). Measurements
1182 for n=2-3 repeats with means are shown. B) Reserve respiratory capacity was calculated as ratio
1183 of (mean maximum)/(mean basal) O2 consumption.

1184 **S4_Fig. Short term treatment with TMZ and RT did not significantly alter DNA methylation**
1185 **pattern of glioblastoma CSCs and SDCs.** Principal component analysis for b-values for all
1186 treatment groups in triplicates for each cell line and differentiation status: HF2303 CSC (A),
1187 HF2303 SDCs (B), HF2927 CSCs (C), and HF2927 SDCs (D).

1188 **S1 Table. Reverse Phase Protein Array (RPPA) Targets, Values, Signaling**
1189 **Pathways**

1190 **S2 Table. Differentially expressed gene lists**

1191 **S3 Table. Interferon signaling correlation group in glioblastoma (TCGA)**

1192 **S4 Table. Differentially methylated probes**

1193

1194

1195

1196

1197

1198

1199

1200

1201

1202

FIGURES AND LEGENDS

A

Patient-derived model ID	Clinical and demographic								Molecular										
	Pathology	Treatment status at collection	Sex	Age @ diagnosis	Rx1	TTP1 (days)	OS (days)	MGMT promoter	TP53	MDM2	CDKN2A	CDK4	EGFR	MET	PTEN	NF1	MYC	Transcriptional subclass	Molecular profiling consortium ID
HF2303	GS	untreated	M	62	RT/ TMZ	88	317	U	p.G245S	0	0	0	0	0	p.D92E	p.W561R	0	Mesenchymal	TCGA-06-0190
HF2354	GBM	BCNU	M	61	RT/ TMZ	60	196	U	p.V216L	0	HOM DEL	0	0	0	splice mut	WT	AMP	ND	n/a
HF2587	GBM	untreated	F	56	RT/ TMZ	232	360	M	WT	0	HOM DEL	0	0	0	p.Q298*	p.W267*	0	Proneural	n/a
HF2927	GBM	untreated	F	55	RT/ TMZ	555	664	M	WT	0	HOM DEL	0	AMP, vIII	0	HOM DEL	WT	0	Classical	n/a
HF3016	GBM	untreated	M	45	RT/ TMZ	88	646	U	p.M133T	0	0	AMP	AMP	0	p.I122S	WT	AMP	Proneural	GLSS-HF-3016-TP
HF3035	GBM	untreated	F	54	RT/ TMZ	196	352	M	WT	0	HOM DEL	0	0	AMP	HOM DEL	WT	0	Classical	n/a
HF3055	GBM	untreated	M	58	RT/ TMZ	77	371	U	WT	AMP	0	AMP	AMP	0	HOM DEL	WT	0	Classical	n/a
HF3077	GBM	untreated	F	56	RT/ TMZ	54	465	M	p.G266E	0	HOM DEL	0	0	AMP	WT	p.R2637*	0	Proneural	n/a

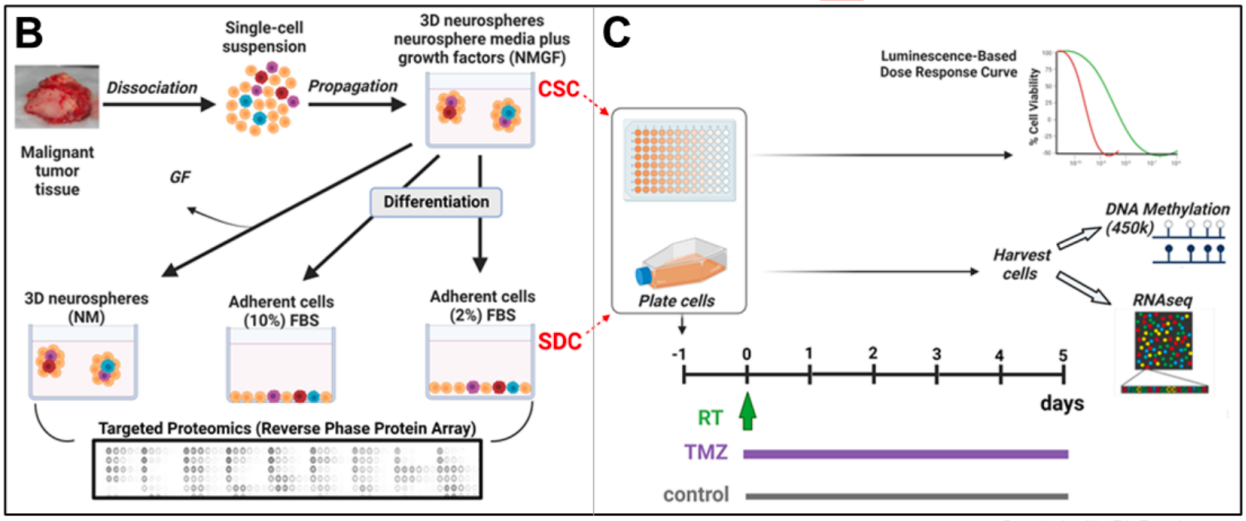

Created with BioRender.com

Fig 1. Glioblastoma patient-derived models and experimental design. A) Clinical and molecular data associated with the GBM patient-derived models. GS, Gliosarcoma; M/F, male/female; RT, radiation therapy; TMZ, temozolomide; Rx1, first-line therapy; TTP, time to progression; OS, overall survival; U/M, unmethylated/methylated MGMT promoter. Red outline denotes extrachromosomal (ecDNA) amplification. MDM2, Mouse double minute 2 homolog; CDKN2A, cyclin-dependent kinase inhibitor 2A; NF1, Neurofibromin 1; MYC family, MYC proto-oncogene, bHLH transcription factor; ND, not determined; AMP, amplification; mut, mutation; hom del, homozygous deletion; WT, wild type; 0, diploid. **B)** Schematic depicting neurosphere culture in NMGF media for selection and amplification of cancer stem cells (CSCs) from surgical specimens, followed by 2 weeks incubation in altered conditions: withdrawal of growth factors (NM), and addition of 2% or 10% FBS. For the purposes of this study, serum-differentiated cells (SDC) are CSCs progeny cultured in NMGF supplemented with 2% FBS. The effect of the different culture conditions on cell signaling were compared by RPPA. **C)** The sensitivity of CSC and SDC to single dose radiation (RT) or 5-day TMZ was measured in three select models. Transcriptional and epigenomic reprograming in SDC vs CSC, and in response to treatment were evaluated by bulk RNAseq and 450k DNA methylation array.

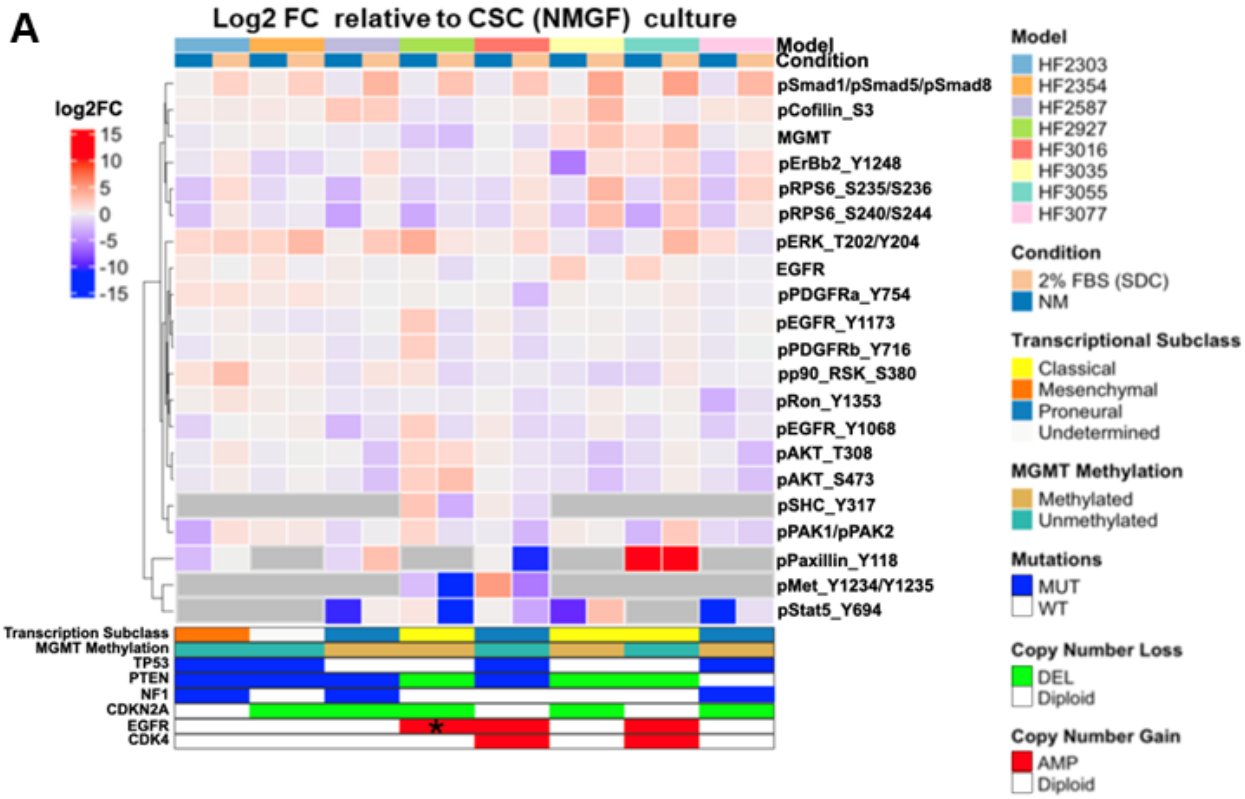

B

	pEGFR_Y1068	pPDGFRb_Y716	pSrc_Y416	pSrc_Y527	pStat3_S727	p-Smad1/5/8	pAKT_S473	pAKT_T308	pGSK3a/b_S21/S9	pmTOR_S2448	pp70_S6K_T412	pRPS6_S235/S236	pRPS6_S240/S244	pP38_T180/Y182	pp90_RSK_S380	pErk_T202/Y204	pAMPKa1_S485	pAMPKb1_S108	pIRS1_S612	pFKHR_S256
pEGFR_Y1068	1.0	0.9	0.3	0.3	0.3	-0.1	-0.2	-0.2	-0.3	0.2	-0.2	-0.2	-0.3			-0.1	0.1		-0.1	-0.2
pPDGFRb_Y716	0.9	1.0	0.3	0.3	0.3	-0.1	-0.2	-0.2	-0.3	0.2	-0.2	-0.2	-0.2		0.1	-0.1	0.1	0.1	-0.1	-0.3
pSrc_Y416	0.3	0.3	1.0	0.7	0.3	-0.1	-0.2	-0.1		0.2	0.3	0.3	0.2	0.3	0.2	0.1		0.4	-0.1	0.2
pSrc_Y527	0.3	0.3	0.7	1.0	0.1	-0.2	-0.3	-0.2		0.3		0.2	0.1		-0.1	-0.2	-0.1	0.4	-0.1	0.3
pStat3_S727	0.3	0.3	0.3	0.1	1.0	0.1	-0.3	-0.3		0.6	0.7	0.4	0.4	0.4	0.7		0.5	0.6	0.3	0.5
p-Smad1/5/8	-0.1	-0.1	-0.1	-0.2	0.1	1.0	-0.4	-0.4	-0.4		0.1	0.5	0.5	0.3	-0.2	0.1	-0.1	0.1	0.3	
pAKT_S473	-0.2	-0.2	-0.2	-0.3	-0.3	-0.4	1.0	1.0	0.8	-0.1	0.1	-0.2	-0.1		0.2	0.5	0.4	-0.2	0.1	
pAKT_T308	-0.2	-0.2	-0.1	-0.2	-0.3	-0.4	1.0	1.0	0.8	-0.1	0.1	-0.2	-0.1		0.1	0.6	0.4	-0.2	0.1	
pGSK3a/b_S21/S9	-0.3	-0.3				-0.4	0.8	0.8	1.0	0.2	0.3	0.1	0.2		0.4	0.5	0.6	0.1	0.4	0.4
pmTOR_S2448	0.2	0.2	0.2	0.3	0.6		-0.1	-0.1	0.2	1.0	0.6	0.6	0.6	0.4	0.4	-0.2	0.4	0.9	0.1	0.5
pp70_S6K_T412	-0.2	-0.2	0.3		0.7	0.1	0.1	0.1	0.3	0.6	1.0	0.7	0.7	0.6	0.6	0.1	0.5	0.6	0.2	0.5
pRPS6_S235/S236	-0.2	-0.2	0.3	0.2	0.4	0.5	-0.2	-0.2	0.1	0.6	0.7	1.0	1.0	0.5	0.2	-0.1	0.2	0.6	0.3	0.5
pRPS6_S240/S244	-0.3	-0.2	0.2	0.1	0.4	0.5	-0.1	-0.1	0.2	0.6	0.7	1.0	1.0	0.4	0.2	-0.1	0.3	0.6	0.4	0.6
pP38_T180/Y182			0.3		0.4	0.3				0.4	0.6	0.5	0.4	1.0	0.4	0.3	0.2	0.5	0.1	0.1
pp90_RSK_S380		0.1	0.2	-0.1	0.7	-0.2	0.2	0.1	0.4	0.4	0.6	0.2	0.2	0.4	1.0	0.3	0.7	0.5	0.4	0.6
pErk_T202/Y204	-0.1	-0.1	0.1	-0.2		0.1	0.5	0.6	0.5	-0.2	0.1	-0.1	-0.1	0.3	0.3	1.0	0.4	-0.1	0.3	0.1
pAMPKa1_S485	0.1	0.1		-0.1	0.5	-0.1	0.4	0.4	0.6	0.4	0.5	0.2	0.3	0.2	0.7	0.4	1.0	0.3	0.5	0.5
pAMPKb1_S108		0.1	0.4	0.4	0.6	0.1	-0.2	-0.2	0.1	0.9	0.6	0.6	0.6	0.5	0.5	-0.1	0.3	1.0	0.1	0.6
pIRS1_S612	-0.1	-0.1	-0.1	-0.1	0.3	0.3	0.1	0.1	0.4	0.1	0.2	0.3	0.4	0.1	0.4	0.3	0.5	0.1	1.0	0.6
pFKHR_S256	-0.2	-0.3	0.2	0.3	0.5				0.4	0.5	0.5	0.5	0.6	0.1	0.6	0.1	0.5	0.6	0.6	1.0

Spearman correlation coefficient (r)

1.0
0.5
0
-0.5
-1.0

Fig 2. Targeted proteomics reveals common and cell specific alterations in key signaling CSCs in response to differentiation and identifies interdependencies in activation of key signaling mediators. A) Heatmap depicting log2 fold change (FC) relative to NMGF (CSC) for the top 5% most variable proteins/PTM. Each value represents mean log2FC for n=3 RPPA measurements/group. Proteins/PTMs which were not detected under all three culture conditions were filtered out for each model (grey cells). MUT, mutation; WT, wild type; AMP, amplification; DEL, deletion **B)** Heatmap of Spearman correlation coefficient values comparing phosphorylation levels in key cell signaling mediators in 8 patient derived GBM models grown in 4 media conditions in triplicates.

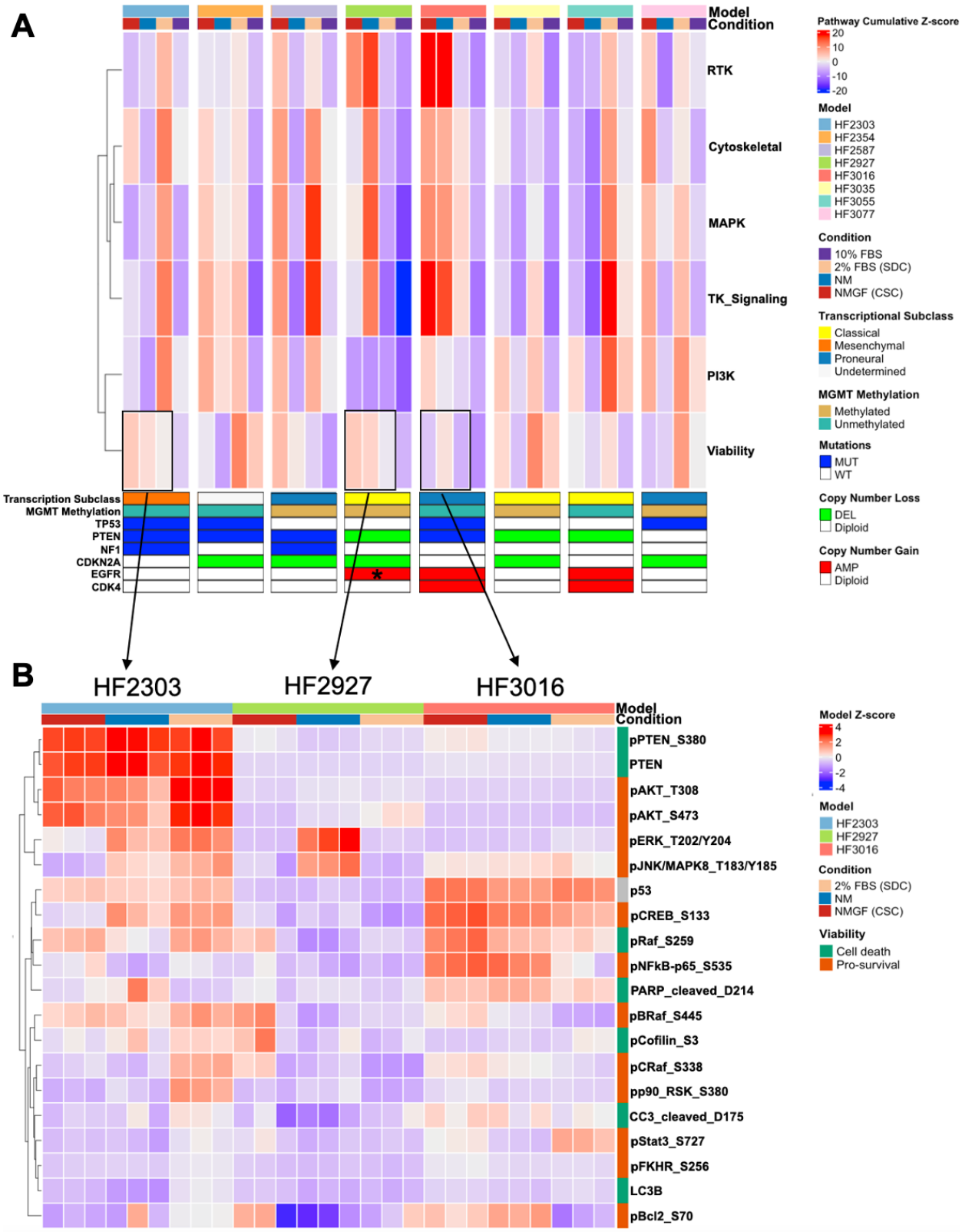

Fig 3. Comparative targeted proteomics of CSCs growing in 4 different conditions. A) Heatmap depicting mean signaling pathway activation for triplicate samples in 4 culture

conditions, for CSCs derived from 8 patients with diverse genomic landscape, transcriptional subclass and MGMT promoter methylation. Hierarchical clustering of rows was based on Spearman correlation analysis. **B)** Heatmap for protein/PTM z-scores involved in cell death and survival signaling for 3 models grown in NMGF (CSC), NM and 2% FBS (SDC), in triplicate (boxes in (A)).

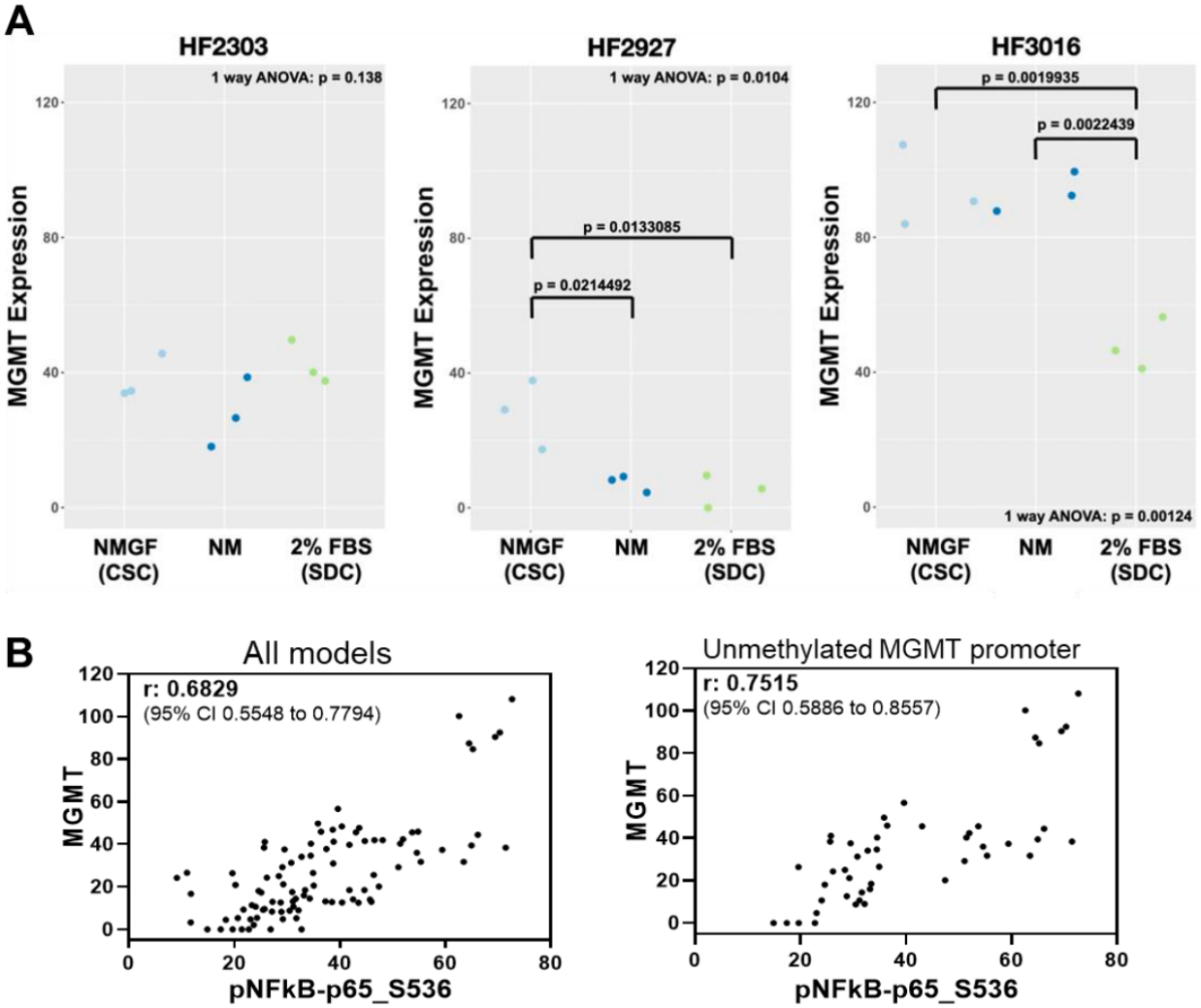

Fig 4. The impact of culture conditions on MGMT protein expression is cell line specific and correlates with NF-kB activation. A) MGMT protein levels measured by RPPA for HF2303, HF2927 and HF3016, in biological triplicates (S1 Table). P-values for 1-way ANOVA and post-hoc TukeyHSD test for comparison of the effect of culture conditions on MGMT protein expression are shown. Pairwise comparison between culture conditions was only significant for HF2927 and HF3016. **B)** Correlation of the levels of MGMT and phospho-NFkB (S536), for all 8 GBM models and culture conditions (left panel) and for the 4 models presenting unmethylated MGMT promoter (right panel). Spearman r and 95% CI are shown.

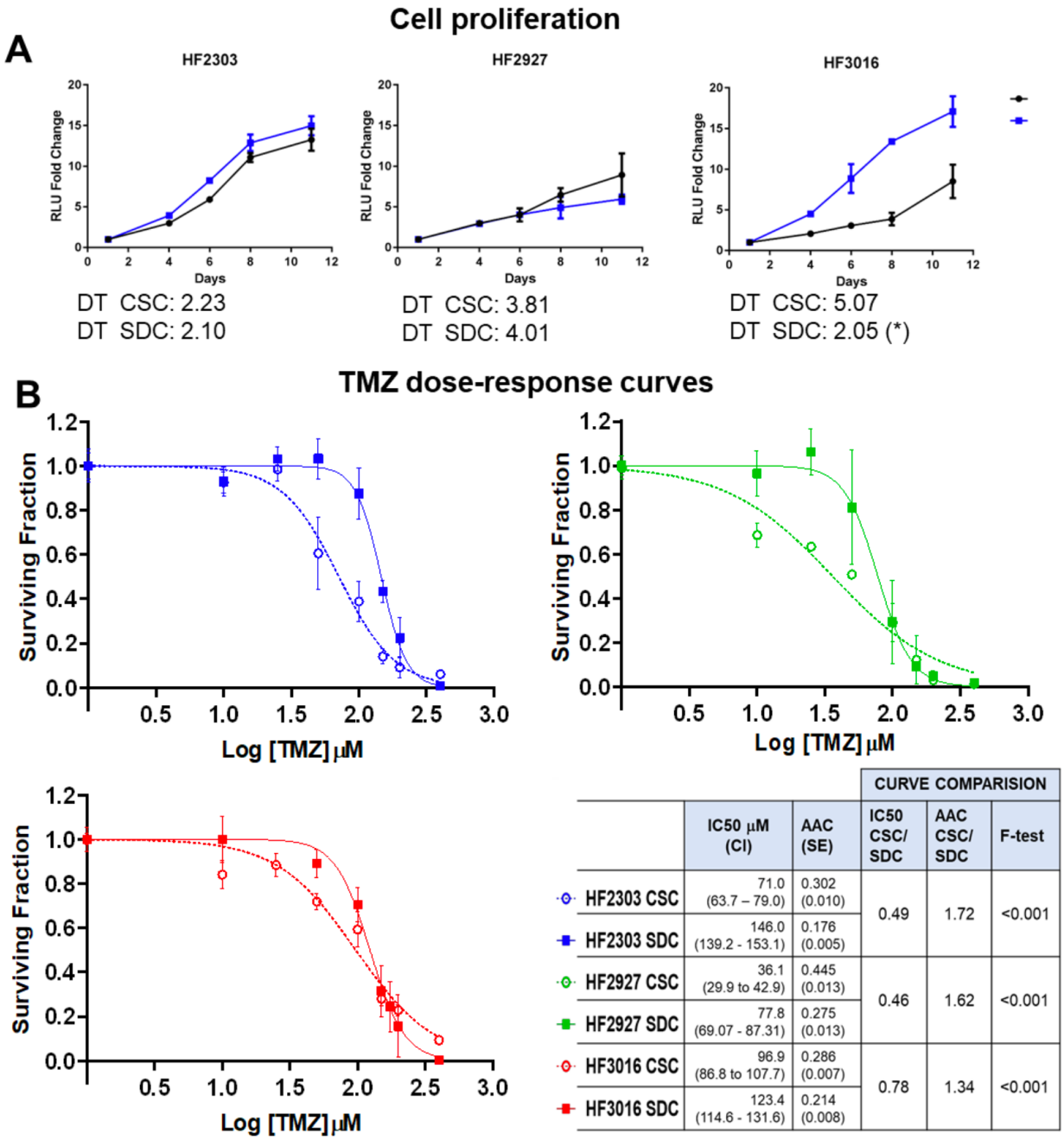

	IC50 µM (CI)	AAC (SE)	CURVE COMPARISION IC50 CSC/ SDC	AAC CSC/ SDC	F-test
HF2303 CSC	71.0 (63.7 – 79.0)	0.302 (0.010)	0.49	1.72	<0.001
HF2303 SDC	146.0 (139.2 - 153.1)	0.176 (0.005)			
HF2927 CSC	36.1 (29.9 to 42.9)	0.445 (0.013)	0.46	1.62	<0.001
HF2927 SDC	77.8 (69.07 - 87.31)	0.275 (0.013)			
HF3016 CSC	96.9 (86.8 to 107.7)	0.286 (0.007)	0.78	1.34	<0.001
HF3016 SDC	123.4 (114.6 - 131.6)	0.214 (0.008)			

Fig 5. GBM CSCs are more sensitive to temozolomide than SDCs. A) To compare cell proliferation rates, CSCs and SDCs for each line were plated in the respective media in 96-well assay plates (1,000 cells/well) and cell viability was measured over 11 days in culture (n=5). Graphs represent mean (SE). The calculated doubling-times (DT, days) are shown, pairwise comparison between CSC and SDC values were significant for HF3016 only (*) $p<0.01$. **B)** Cells were plated in 96-well assay plates (2,000/plate) and treated for 5 days with the indicated doses of temozolomide, or equivalent DMSO control. Dose-response curves, the calculated IC50 concentrations with confidence interval (CI), and area above the curve (AAC) expressed as a fraction of total area with SE are shown. For each of the GBM patients, CSCs were significantly more sensitive to TMZ relative to SDCs, as shown by IC50 and AAC ratios, and p-values for dose-response curve comparison (F-test).

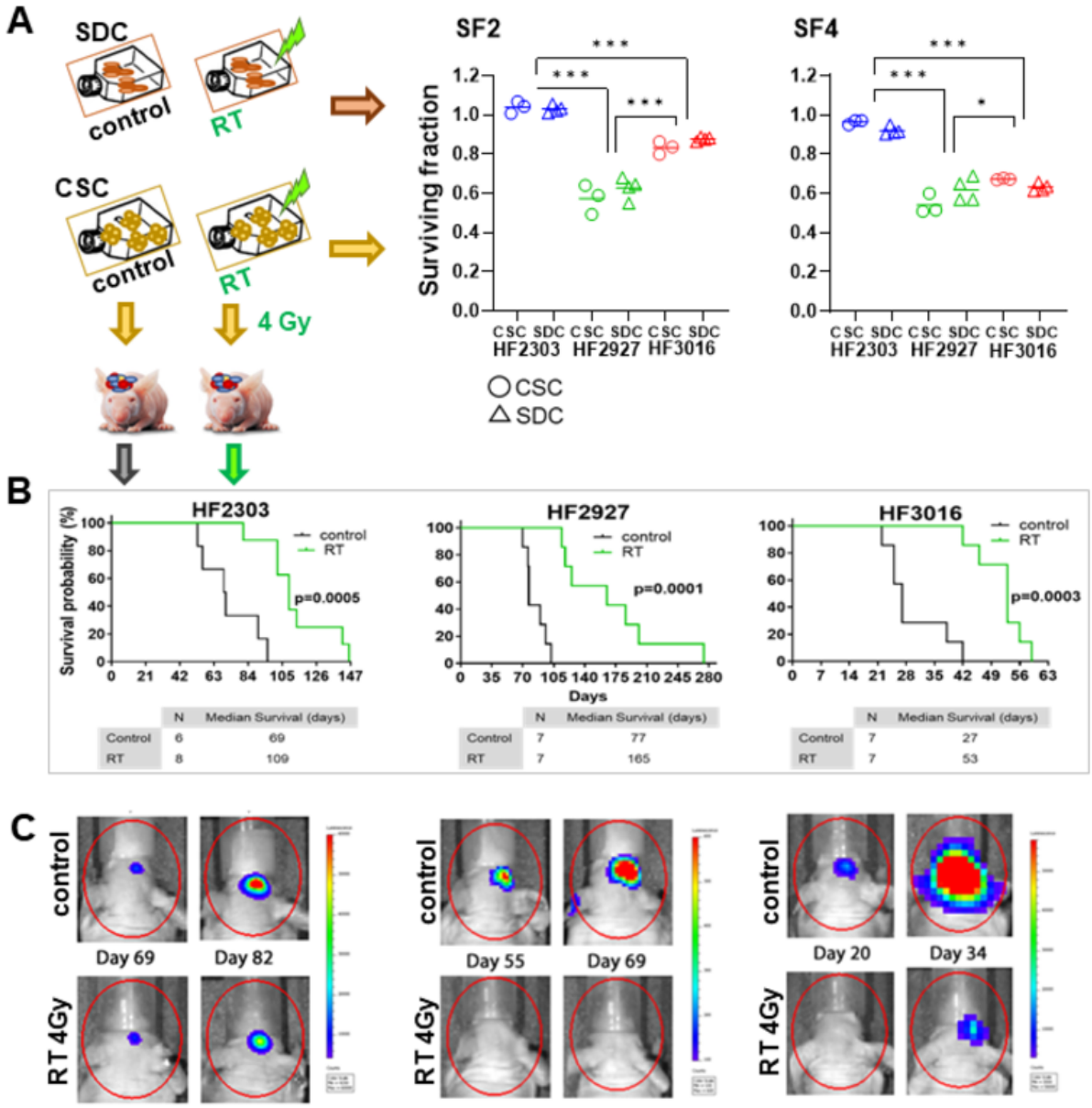

Fig 6. Response of glioblastoma CSCs and SDCs to ionizing radiation. **A)** CSC and SDC received a single radiation dose (2Gy or 4Gy) or mock radiation (control), and cell viability was measured 5 days later (n=3-4). No significant difference in sensitivity to RT between CSC and SDCs was observed for any of the lines (Holm-Sidak multiple comparisons test with adj p-value<0.05 threshold). The surviving fraction (SF) values among the 3 cell lines (CSC and SDC combined) were compared by one-way ANOVA, followed by Tukey's multiple comparisons tests, adj p value<0.0001(***), <0.05 (*). **B)** Irradiated and control CSCs were implanted intracranially immediately after treatment, $3x10^5$ cells/mouse (n=6-8/group). Symptom-free survival for the orthotopic PDX is shown in Kaplan-Meier curves, compared by log-rank test. **C)** Longitudinal live bioluminescense images for representative PDX in (B).

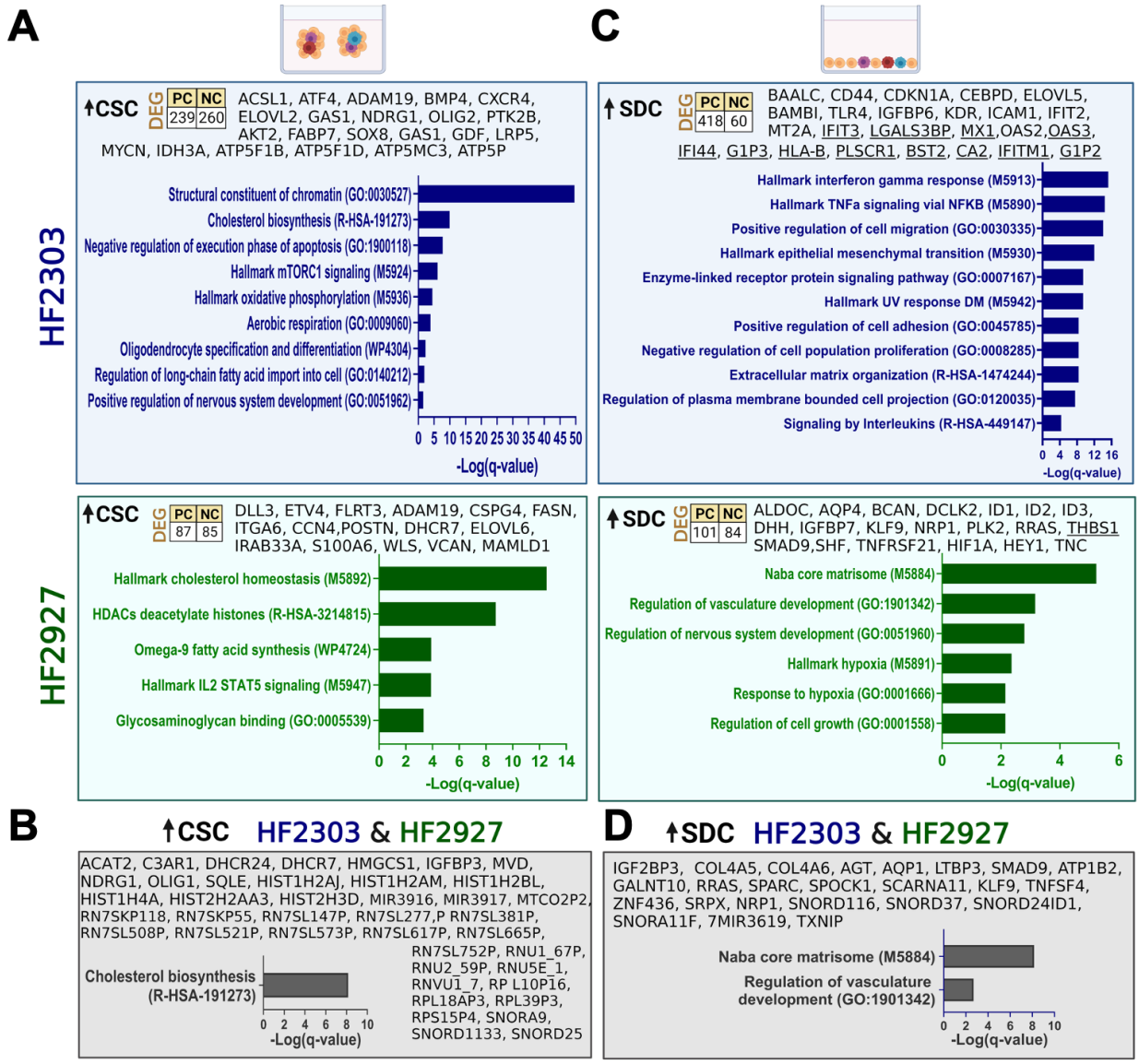

Fig 7. Transcriptional reprograming in glioblastoma cells in response to CSC differentiation. HF2927 and HF2303 CSC were grown in regular neurosphere media or in SDC cultures for 2 weeks. Total RNA from triplicate samples for each group was sequenced analyzed and DEG between CSC and SDC determined for each line. Total number of protein coding (PC) and non-coding (NC) genes, select genes and Metascape gene-set enrichment tests adjusted for multiple comparisons (q-value < 0.05) are shown for genes upregulated in CSCs (A) and in SDCs (C). The common DEGs for both lines along with enriched cellular processes are presented: 43 genes upregulated in CSCs (B) and 25 genes upregulated in SDCs (D).

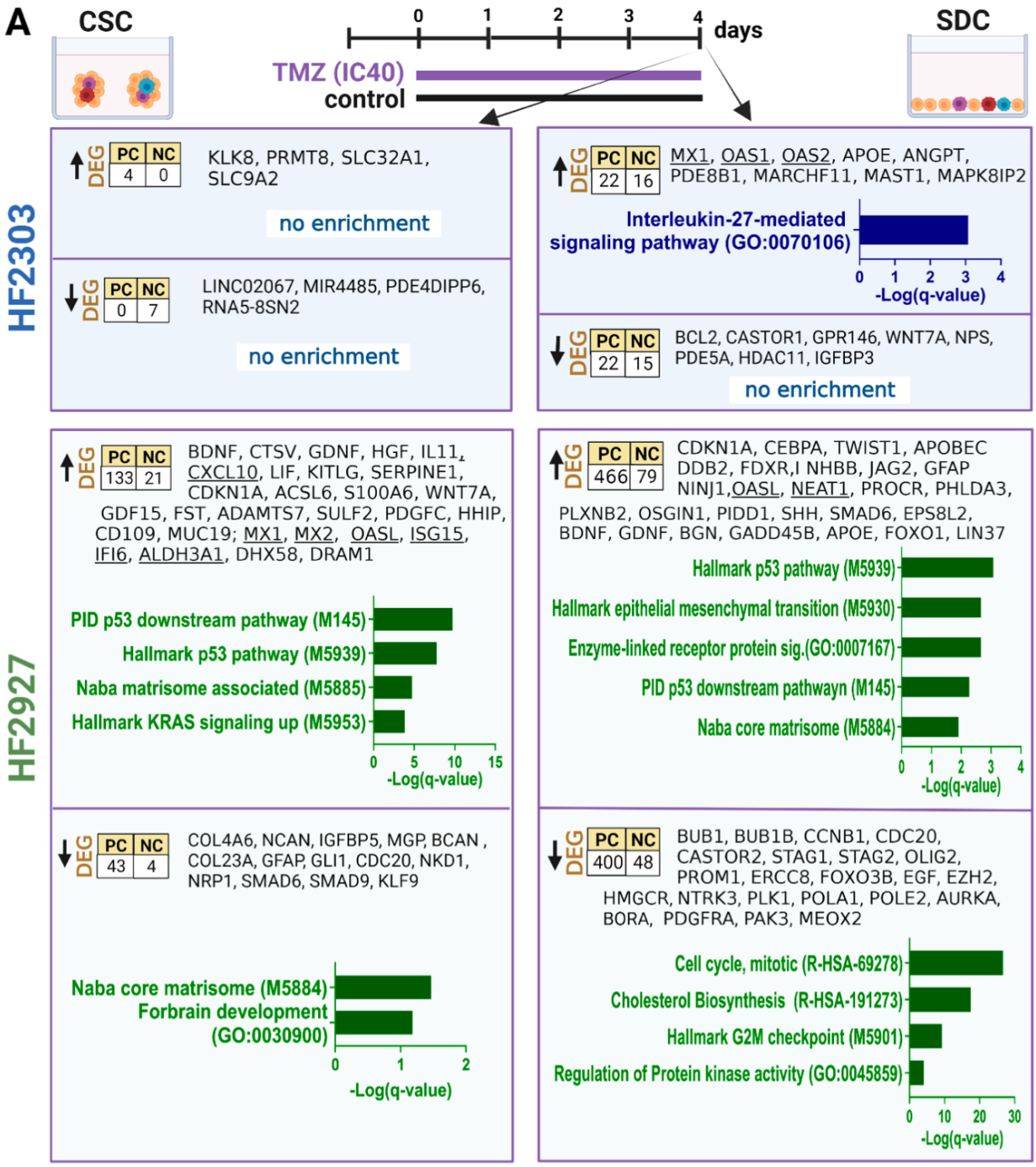
A
CSC
SDC
0
1
2
3
4
days
TMZ (IC40)
control
HF2303
DEG
PC NC
4 0
KLK8, PRMT8, SLC32A1, SLC9A2
no enrichment
DEG
PC NC
0 7
LINC02067, MIR4485, PDE4DIPP6, RNA5-8SN2
no enrichment
DEG
PC NC
22 16
MX1, OAS1, OAS2, APOE, ANGPT, PDE8B1, MARCHF11, MAST1, MAPK8IP2
Interleukin-27-mediated signaling pathway (GO:0070106)
0 1 2 3 4
-Log(q-value)
DEG
PC NC
22 15
BCL2, CASTOR1, GPR146, WNT7A, NPS, PDE5A, HDAC11, IGFBP3
no enrichment
HF2927
DEG
PC NC
133 21
BDNF, CTSV, GDNF, HGF, IL11, CXCL10, LIF, KITLG, SERPINE1, CDKN1A, ACSL6, S100A6, WNT7A, GDF15, FST, ADAMTS7, SULF2, PDGFC, HHIP, CD109, MUC19; MX1, MX2, OASL, ISG15, IFI6, ALDH3A1, DHX58, DRAM1
PID p53 downstream pathway (M145)
Hallmark p53 pathway (M5939)
Naba matrisome associated (M5885)
Hallmark KRAS signaling up (M5953)
0 5 10 15
-Log(q-value)
DEG
PC NC
466 79
CDKN1A, CEBPA, TWIST1, APOBEC DDB2, FDXR,I NHBB, JAG2, GFAP NINJ1,OASL, NEAT1, PROCR, PHLDA3, PLXNB2, OSGIN1, PIDD1, SHH, SMAD6, EPS8L2, BDNF, GDNF, BGN, GADD45B, APOE, FOXO1, LIN37
Hallmark p53 pathway (M5939)
Hallmark epithelial mesenchymal transition (M5930)
Enzyme-linked receptor protein sig.(GO:0007167)
PID p53 downstream pathwayn (M145)
Naba core matrisome (M5884)
0 1 2 3 4
-Log(q-value)
DEG
PC NC
43 4
COL4A6, NCAN, IGFBP5, MGP, BCAN , COL23A, GFAP, GLI1, CDC20, NKD1, NRP1, SMAD6, SMAD9, KLF9
Naba core matrisome (M5884)
Forbrain development (GO:0030900)
0 1 2
-Log(q-value)
DEG
PC NC
400 48
BUB1, BUB1B, CCNB1, CDC20, CASTOR2, STAG1, STAG2, OLIG2, PROM1, ERCC8, FOXO3B, EGF, EZH2, HMGCR, NTRK3, PLK1, POLA1, POLE2, AURKA, BORA, PDGFRA, PAK3, MEOX2
Cell cycle, mitotic (R-HSA-69278)
Cholesterol Biosynthesis (R-HSA-191273)
Hallmark G2M checkpoint (M5901)
Regulation of Protein kinase activity (GO:0045859)
0 10 20 30
-Log(q-value)

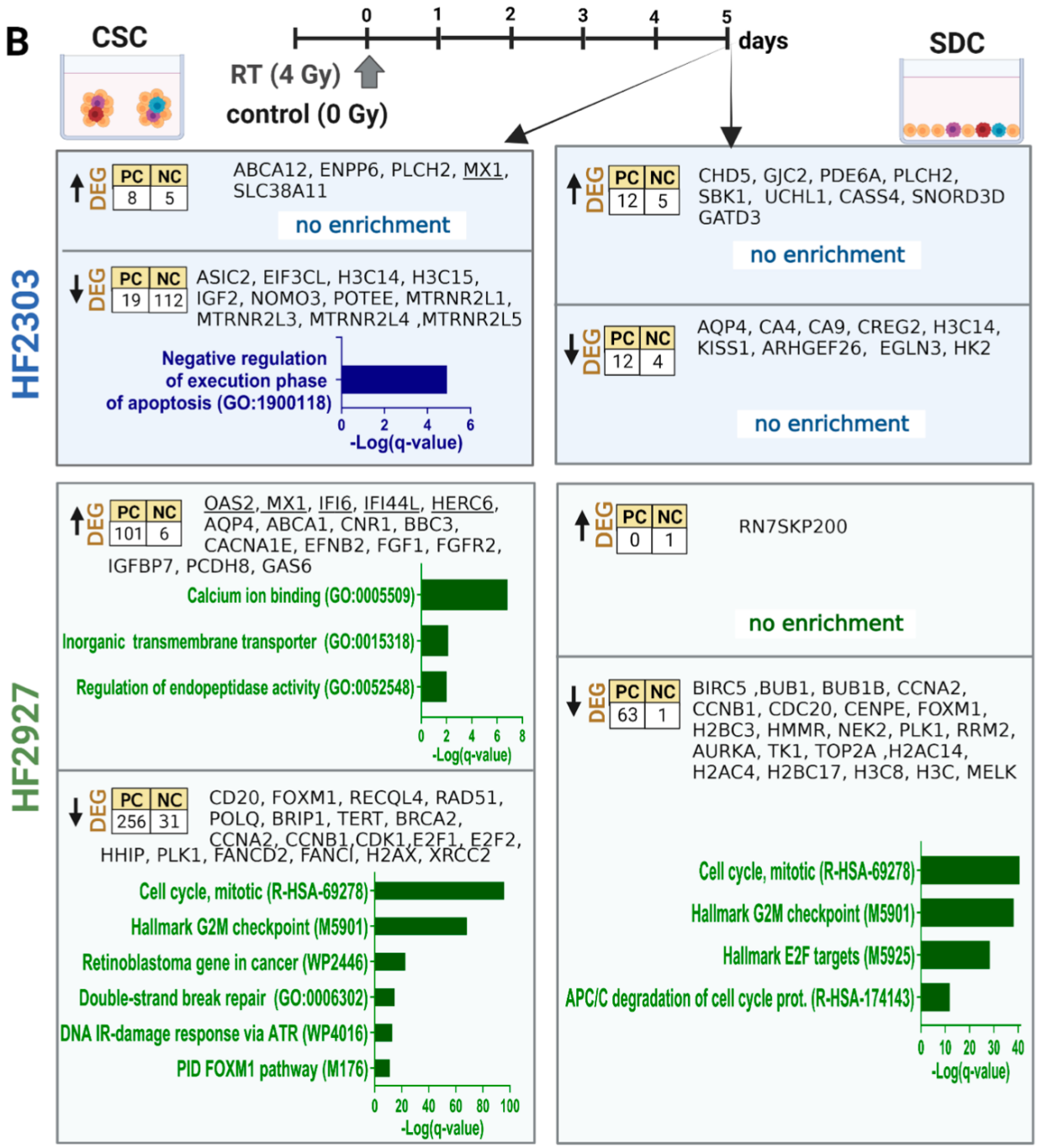
B
CSC
SDC
0
1
2
3
4
5
days
RT (4 Gy)
control (0 Gy)
HF2303
DEG
PC NC
8 5
ABCA12, ENPP6, PLCH2, MX1, SLC38A11
no enrichment
DEG
PC NC
19 112
ASIC2, EIF3CL, H3C14, H3C15, IGF2, NOMO3, POTEE, MTRNR2L1, MTRNR2L3, MTRNR2L4 ,MTRNR2L5
Negative regulation of execution phase of apoptosis (GO:1900118)
0 2 4 6
-Log(q-value)
DEG
PC NC
12 5
CHD5, GJC2, PDE6A, PLCH2, SBK1, UCHL1, CASS4, SNORD3D GATD3
no enrichment
DEG
PC NC
12 4
AQP4, CA4, CA9, CREG2, H3C14, KISS1, ARHGEF26, EGLN3, HK2
no enrichment
HF2927
DEG
PC NC
101 6
OAS2, MX1, IFI6, IFI44L, HERC6, AQP4, ABCA1, CNR1, BBC3, CACNA1E, EFNB2, FGF1, FGFR2, IGFBP7, PCDH8, GAS6
Calcium ion binding (GO:0005509)
Inorganic transmembrane transporter (GO:0015318)
Regulation of endopeptidase activity (GO:0052548)
0 2 4 6 8
-Log(q-value)
DEG
PC NC
256 31
CD20, FOXM1, RECQL4, RAD51, POLQ, BRIP1, TERT, BRCA2, CCNA2, CCNB1,CDK1,E2F1, E2F2, HHIP, PLK1, FANCD2, FANCI, H2AX, XRCC2
Cell cycle, mitotic (R-HSA-69278)
Hallmark G2M checkpoint (M5901)
Retinoblastoma gene in cancer (WP2446)
Double-strand break repair (GO:0006302)
DNA IR-damage response via ATR (WP4016)
PID FOXM1 pathway (M176)
0 20 40 60 80 100
-Log(q-value)
DEG
PC NC
0 1
RN7SKP200
no enrichment
DEG
PC NC
63 1
BIRC5 ,BUB1, BUB1B, CCNA2, CCNB1, CDC20, CENPE, FOXM1, H2BC3, HMMR, NEK2, PLK1, RRM2, AURKA, TK1, TOP2A ,H2AC14, H2AC4, H2BC17, H3C8, H3C, MELK
Cell cycle, mitotic (R-HSA-69278)
Hallmark G2M checkpoint (M5901)
Hallmark E2F targets (M5925)
APC/C degradation of cell cycle prot. (R-HSA-174143)
0 10 20 30 40
-Log(q-value)

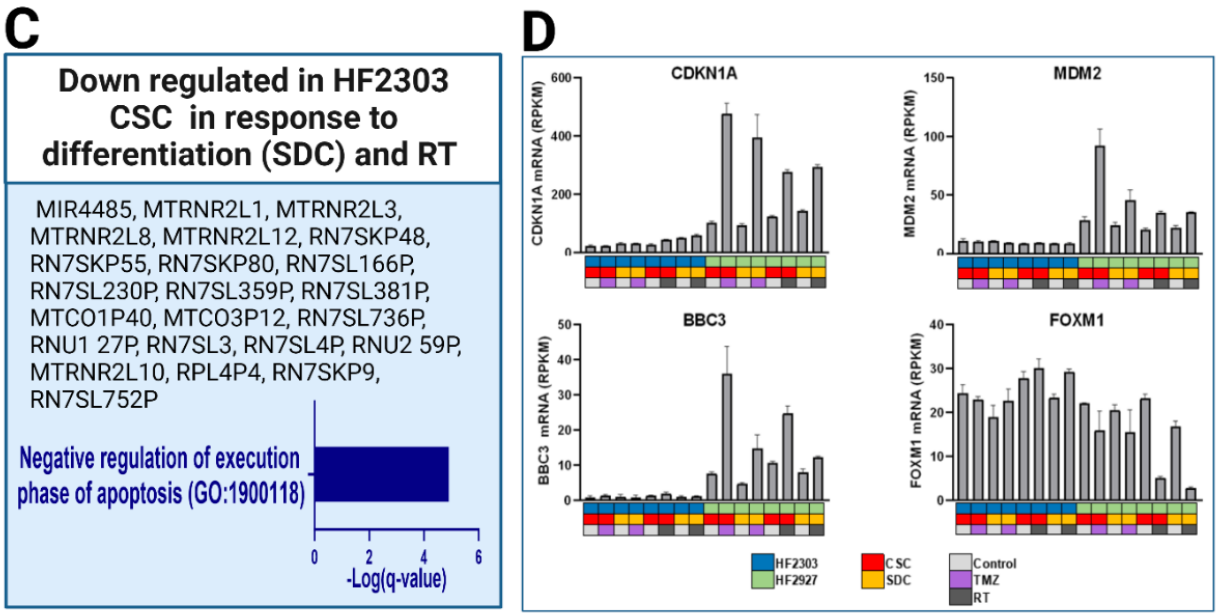

Fig 8. Transcriptional response to genotoxic treatment in glioblastoma cells. Differentially expressed genes between treated and control samples were determined and enrichment performed as described for Fig. 7. **A)** Transcriptional changes in CSCs and SDCs in response to 4-day TMZ treatment (IC40 concentrations). **B)** Transcriptional changes in CSCs and SDCs measured 5 days after one dose RT (4 Gy). **C)** RNA commonly downregulated in HF2303 CSCs in response to differentiation and RT treatment. **D)** mRNA expression (RPKM) of p53 transcriptional targets CDKN1A (p21), MDM2, and BBC3, and of cell cycle regulators in HF2303 and HF2927 control and treated cells, mean and SE of n=3. Figures created with Biorender.com.

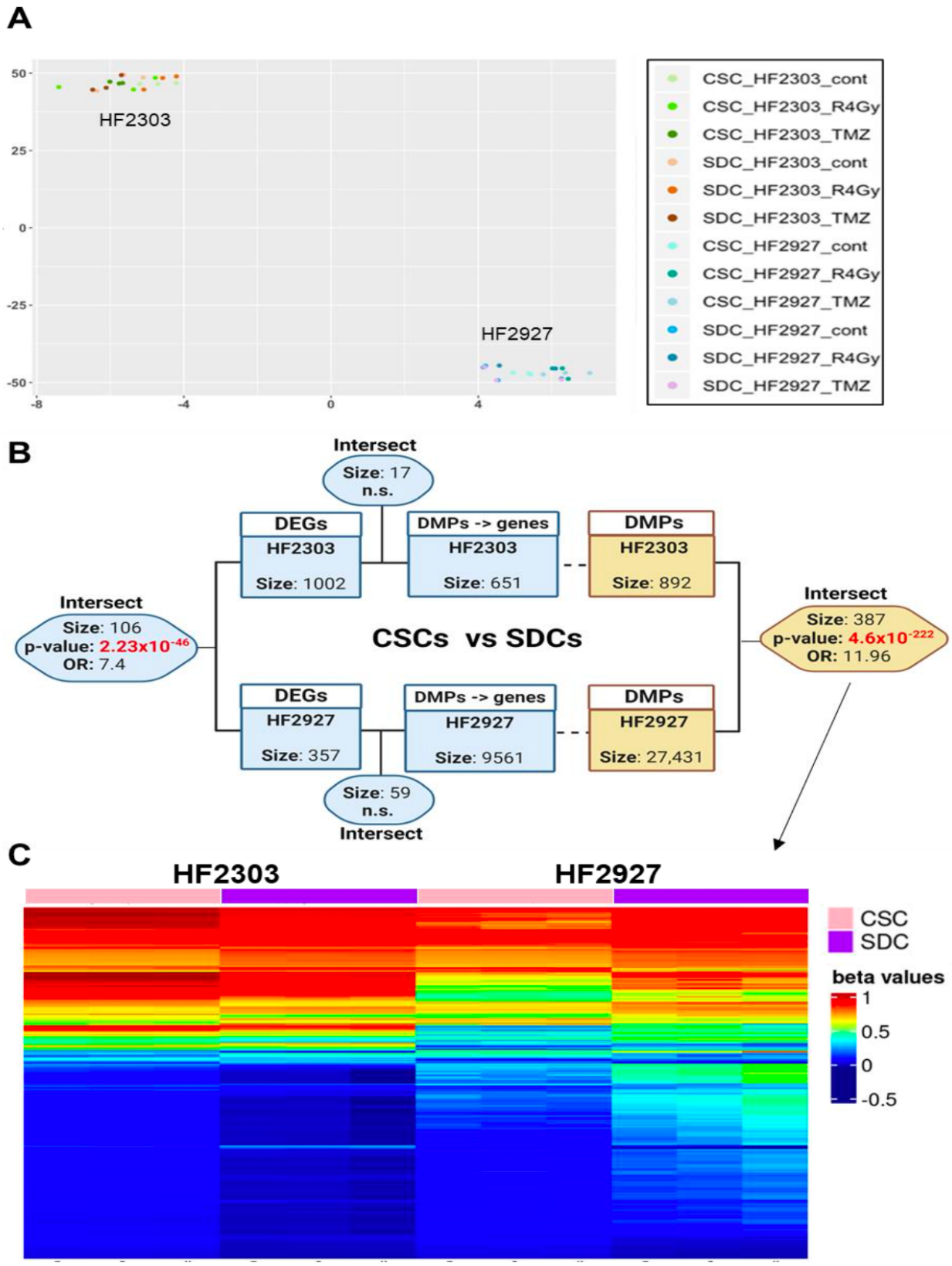
A
HF2303
HF2927
CSC_HF2303_cont
CSC_HF2303_R4Gy
CSC_HF2303_TMZ
SDC_HF2303_cont
SDC_HF2303_R4Gy
SDC_HF2303_TMZ
CSC_HF2927_cont
CSC_HF2927_R4Gy
CSC_HF2927_TMZ
SDC_HF2927_cont
SDC_HF2927_R4Gy
SDC_HF2927_TMZ
B
Intersect
Size: 17
n.s.
DEGs
HF2303
Size: 1002
DMPs -> genes
HF2303
Size: 651
DMPs
HF2303
Size: 892
Intersect
Size: 106
p-value: 2.23x10-46
OR: 7.4
CSCs vs SDCs
Intersect
Size: 387
p-value: 4.6x10-222
OR: 11.96
DEGs
HF2927
Size: 357
DMPs -> genes
HF2927
Size: 9561
DMPs
HF2927
Size: 27,431
Size: 59
n.s.
Intersect
C
HF2303
HF2927
CSC
SDC
beta values
1
0.5
0
-0.5

Fig 9. Genome-wide DNA methylation profiling groups samples by patient of origin and identifies DNA methylation alteration patterns between glioblastoma CSCs and their SDCs progeny. A) t-distributed stochastic neighbor embedding (t-SNE) plot from b-values for all CpG sites comparing HF2303 and HF2927 CSCs and SDCs treated with control, RT or TMZ, in triplicates. **B)** Schematic showing the significant intersect for HF2303 and HF2927 of differentially expressed genes (DEGs) and differentially methylated positions (DMPs) between CSCs and SDCs. The intersect between DMPs mapped to genes (see Methods) and DEGs are shown. Significance of the intersections was determined using GeneOverlap, p-values and estimated odds ratio are shown; n.s., nonsignificant. **C)** Heatmap showing the b-values for the 387 DMPs common to HF2303 and HF2927. Figure 9B was created with Biorender.com.